Two-Dimensional Model for the Martian Exosphere: Applications to Hydrogen and Deuterium Lyman α Observations

D. Bhattacharyya[1], J. Y. Chaufray[2], M. Mayyasi[1], J. T. Clarke[1], S. Stone[3], R. V. Yelle[3], W. Pryor[4], J. L Bertaux[2], J. Deighan[5], S. K. Jain[5], and N. M. Schneider[5]

1. *Center for Space Physics, Boston University, 725 Commonwealth Avenue, Boston MA 02215, USA*
2. *LATMOS/CNRS, 78280 Guyancourt, France*
3. *Lunar and Planetary Laboratory, University of Arizona, 1629 E University Blvd., Tucson AZ 80092, USA*
4. *Science Division, Central Arizona College, Coolidge, AZ 85128, USA*
5. *Laboratory of Atmospheric and Space Physics, Boulder, CO 80303, USA*

To be submitted to *Icarus*

43 Pages

1 Table

7 Figures

Proposed running title: 2-D radiative transfer model for Mars

Corresponding author address:
Dolon Bhattacharyya
Center for Space Physics
Boston University
725 Commonwealth Avenue
Boston MA 02215, USA
e-mail: dolonb@bu.edu

Abstract

The analysis of Lyman α observations in the exosphere of Mars has become limited by the assumption of spherical symmetry in the modeling process, as the models are being used to analyze increasingly detailed measurements. In order to overcome this limitation, a two-dimensional density model is presented, which better emulates the density distribution of deuterium and hydrogen atoms in the exosphere of Mars. A two-dimensional radiative transfer model developed in order to simulate multiple scattering of solar Lyman α photons by an asymmetric, non-isothermal hydrogen exosphere, is also presented here. The models incorporate changes in density and temperature structure of the martian atmosphere with radial distance and solar zenith angle. The 2-D models were applied to the MAVEN-IUVS echelle observations of deuterium and hydrogen Lyman α as well as HST Lyman α observations of hydrogen at Mars. The asymmetric 2-D model provided better fits to the data and smaller thermal escape rates in comparison to the symmetric 1-D model for the exosphere of Mars. However, intensity differences between both models became small above ~2.5 martian radii indicating that the exosphere of Mars approaches spherical symmetry at higher altitudes, in agreement with earlier studies. In addition, a new cross calibration of the absolute sensitivities of two instruments on the Hubble Space Telescope and the MAVEN-IUVS echelle mode is presented based on near-simultaneous observations of the geocorona and Mars.

Keywords: Mars; Atmosphere; Ultraviolet observations; Radiative transfer

1. Introduction

Resonantly scattered solar Lyman α photons by martian exospheric hydrogen have been studied for decades before the transition into 21st century [Barth et al., 1969, 1971; Anderson and Hord, 1971, 1972; Babichenko et al., 1976; Dostovalov and Chuvakhin, 1973]. This Lyman α emission at 1215.67 Å was observed to extend to very high altitudes, beyond 30,000 km (~ 8.8 R_{Mars}) [Barth et al., 1969]. Photochemical modeling indicated that most of the exospheric H atoms originated from the photo-dissociation of water vapor by ultraviolet sunlight close to the planet's surface [Hunten and McElroy, 1970; McElroy and Donahue, 1972; Parkinson and Hunten, 1972]. This realization piqued an interest towards understanding the properties of martian exospheric hydrogen as it could provide an insight into the disappearance of Mars' water. Since the majority of H atoms at Mars were theorized to be escaping by the thermal mechanism of Jeans escape [Hunten, 1973, 1982], knowledge about the density distribution and the temperature of the H atoms was deemed necessary to constrain the present-day escape rate of H/H_2O from Mars.

Observations of the martian Lyman α emission conducted in the past decade revealed significant seasonal changes in H escape rate, with the peak escape occurring close to Mars' southern summer solstice ($L_s = 270^\circ$) [Clarke et al., 2014; 2017; Chaffin et al., 2014; Bhattacharyya et al., 2015; 2017b; Romanelli et al., 2016; Halekas et al., 2017; Rahmati et al., 2017; 2018]. These large seasonal changes were not expected from earlier photochemical modeling of the martian atmosphere [Hunten 1973; Krasnopolsky 2002], and are believed to be a result of a combination of atmospheric upwelling and dust storm activity lifting water vapor to higher altitudes around Mars' perihelion [Chaffin et al., 2017; Fedorova et al., 2017; Heavens et al., 2018; Clarke, 2018]. This discovery has implications for understanding the water escape history of Mars. Analysis of the observations also revealed the possibility of the presence of an energetic population of hydrogen along with thermal H in the martian exosphere, which could increase (~factor of 2) the present-day escape rate of hydrogen from Mars [Chaufray et al., 2008; Bhattacharyya et al., 2017a]. More recently, an enhancement in martian hydrogen escape was also detected by the Imaging Ultraviolet Instrument (IUVS) [McClintock et al., 2015] onboard the Mars Atmosphere Volatile EvolutioN (MAVEN) spacecraft during a series of strong solar flare events and a coronal mass ejection that swept past Mars [Mayyasi et al., 2018]. These findings about the martian exosphere in the past decade indicate that the water escape scenario at Mars is complicated, and

all the significant factors that influence hydrogen escape at Mars have to be modeled, analyzed and studied in detail before an accurate estimate of the timeline of Mars's water loss is made.

Lyman α emission from deuterium at 1215.33 Å, the heavier isotope of hydrogen, on the other hand, has only recently been studied in detail to determine the D/H ratio at Mars [Clarke et al., 2017; Mayyasi et al., 2017b; 2019]. The deuterium to hydrogen ratio is a good indicator of a planet's water loss in the past through atmospheric escape. The lightest gases from every terrestrial planet in our solar system are slowly evaporating into space. In the case of hydrogen and its heavier isotope deuterium, hydrogen is escaping much faster than deuterium due to the difference in their masses. Such an escape imbalance over long periods of time would enhance the D/H ratio in a planet's atmosphere, thereby providing an estimate of the amount of atmosphere that has escaped the planet [Bertaux et al., 1993; Krasnopolsky et al., 1998].

Global measurements of D/H ratio through observations of HDO and H_2O in the martian atmosphere revealed it to be 6 ± 3 times higher than the standard mean ocean water (SMOW) value (1.5576×10^{-4}) [Owen et al., 1988] indicating an extended history of atmospheric escape from Mars. A more recent measurement of the martian D/H ratio by the Mars Science Laboratory (MSL) constrained it to be 3 ± 0.2 × SMOW [Mahaffy et al., 2015b]. Further measurement of D/H from observations of H_2O and HDO indicated large latitudinal variations with enhancements of ~7 times SMOW in certain areas, which lent further support to the earlier conclusion of bulk atmospheric loss from Mars [Villanueva et al., 2015]. However, all these measurements were confined to the lower atmosphere (below an altitude of ~60 km) and were indirect estimates of the D/H ratio through HDO and H_2O observations, with the assumption that HDO and H_2O are the major sources of D and H atoms in the martian exosphere. Observations of martian exospheric deuterium Lyman α emission (1215.33 Å) with the IUVS-echelle instrument onboard MAVEN over two Mars years, revealed that deuterium exhibits large seasonal variations like hydrogen, with its peak close to southern summer solstice [Clarke et al., 2017; Mayyasi et al., 2017b; 2019]. This might result in a different D/H ratio for the upper atmosphere. Therefore, it is imperative to combine the deuterium and hydrogen observations with MAVEN and the Hubble Space Telescope (HST) taken in the past decade and use the most advanced modeling techniques in order to obtain the martian exospheric D/H value so as to put accurate constraints on the water and atmospheric loss incurred by Mars over its 4.5-billion-year existence.

153 The MAVEN spacecraft has been in orbit around Mars from September 2014. Since then
154 its various suite of instruments has been studying the martian atmosphere. Images of the Lyman α
155 emission from hydrogen in the martian exosphere have revealed it to be spherically asymmetric in
156 structure [Chaffin et al., 2015]. Similar findings were made with HST [Bhattacharyya et al., 2017a]
157 and Mars Express (MEX) [Holmström, 2006] which found the hydrogen exosphere at Mars to be
158 spherically asymmetric below 2.5 martian radii (~8500 km). The Neutral Gas and Ion Mass
159 Spectrometer (NGIMS) [Mahaffy et al., 2015a] onboard MAVEN has measured atmospheric
160 temperature differences of > 100 K between the day and the night side of Mars [Stone et al., 2018].
161 The MAVEN spacecraft, which had an apoapse of ~6000 km and periapse of ~150 km up until
162 early 2019, conducted observations of martian D and H Lyman α emissions in a region where the
163 exospheric structure is not spherically symmetric. Therefore, earlier models which assumed a
164 spherically symmetric, isothermal exosphere [Anderson and Hord, 1971; Anderson 1974;
165 Chaufray et al., 2008; Chaffin et al., 2014; 2015; 2018; Bhattacharyya et al., 2015; 2017a; 2017b],
166 might not accurately capture the actual physical properties of the H and D atoms at Mars.
167 The large difference in exospheric temperature between day and night at Mars, as observed
168 by MAVEN-NGIMS could affect the model-derived Jeans escape rate of hydrogen when assuming
169 a spherically symmetric atmosphere. For example, a 250 K exobase temperature and 10^4 cm^{-3}
170 density for a symmetric exospheric would result in a Jeans escape rate of 2.01×10^{25} particles/sec
171 for H, which is ~1.86 times higher than the Jeans escape rate from an asymmetric non-isothermal
172 atmosphere, in which the temperature trend follows the NGIMS observations (section 2.1) and the
173 density trend follows the Hodges and Johnson [1968] formulation for light species (section 2.2).
174 Therefore, in this paper, a more physically accurate two-dimensional model of the martian
175 exosphere is presented which is being applied to study the H and D Lyman α emissions from
176 MAVEN and HST in order to provide better constraints on the H escape rates at Mars, which in
177 turn, would help estimate the actual amount of water lost by Mars.
178 Section 2 summarizes the two-dimensional atmosphere model for a non-symmetric, non-
179 isothermal atmosphere unlike the standard Chamberlain model [Chamberlain, 1963] usually used
180 to derive exospheric density distributions of the lightest atomic species for terrestrial planets.
181 Section 3 summarizes the two-dimensional radiative transfer model which accounts for a non-
182 spherical, non-isothermal atmosphere in order to simulate the optically thick H Lyman α emission
183 at Mars. Section 4 presents the application of the asymmetric model to MAVEN and HST

observations as well as comparisons between the symmetric and asymmetric model to MAVEN observations of D and H Lyman α emissions and HST observations of H Lyman α emission. Section 5 presents a discussion and summary of the results and implications of this work towards characterizing the martian exosphere. Appendix A and B details the 2-D atmosphere model as well as the non-spherical, non-isothermal radiative transfer model developed for the analysis of the MAVEN and HST observations.

2. Two-Dimensional density model of the martian exosphere

It was expected, and MEX, HST, and MAVEN data have confirmed, that the martian upper atmosphere is highly asymmetric in density and temperature [Holmström, 2006; Bhattacharyya et al., 2017a; Chaffin et al., 2015; Stone et al., 2018]. This asymmetric nature of the martian exosphere necessitates the usage of models which accounts for a non-symmetric, non-isothermal exosphere while analyzing the data from various instruments. In the modeling process, the exobase density and temperature are varied in the radial direction and with solar zenith angle (SZA) to simulate the martian exosphere. While in the future a more complex local time dependence may be considered in the modeling process, here variation of atmospheric characteristics with only solar zenith angle is considered in an effort to improve the models, as SZA variation is a significant one recorded in the MAVEN data [Stone et al., 2018].

The 2-dimensional density model assumes that the arbitrary altitude at which the atmosphere transitions from the collisional to collisionless regime (exobase altitude) to be 200 km at Mars. The model atmosphere has an upper boundary at 50,000 km and a lower boundary at 80 km. Lyman α is completely absorbed by CO_2 at Mars at altitudes below 80 km. Thus, the region below 80 km is opaque at this UV wavelength, which is why the altitude of 80 km is taken as the lower atmospheric boundary in the modeling process.

The 2-D model has only one free parameter, the exobase density of either thermal D or H at SZA = 0°. The exobase temperature for thermal H/D is pre-determined from existing alternate observations of other neutral species like CO_2 and Ar present in the martian atmosphere. This is necessary as there exists degeneracy between the temperature and density parameters when analyzing optically thick emissions like Lyman α [Bhattacharyya et al., 2017]. Therefore, the accuracy of modeling results is highly dependent on a correct representation of the temperature

structure for the martian atmosphere which necessitated the development of a 2-D model in light of the MAVEN-NGIMS derived temperature differences between the day and night side of Mars.

2.1 Variation of temperature with SZA, solar longitude, and altitude

MAVEN observations of the martian atmosphere made over the course of approximately two Mars years by the NGIMS instrument were used to determine the variation of Mars' exospheric temperature with SZA [Stone et al., 2018]. Figure 1 shows this trend as observed by MAVEN. The black line represents the data averaged over a large number of measurements and the red line is the closest decreasing fit to the data. The small variations in the data is most likely the result of MAVEN's constantly changing viewing geometry combined with changes in solar activity over the two Mars years. The closest decreasing fit eliminates these variations in the data by assuming that the temperature can only decrease with SZA. This delivers a dayside trend agreeable with Mars Global Circulation Models (MGCM) [Bougher et al., 2015; Chaufray et al., 2018]. Given a temperature at SZA = 0˚, the curve depicted by the red line is then used to determine the variation of temperature with SZA. Figure 1 below, which is an adaptation of figure 2 from Mayyasi et al., [2019], has been included in this paper in order to present a more robust discussion of the models which make extensive use of this temperature trend.

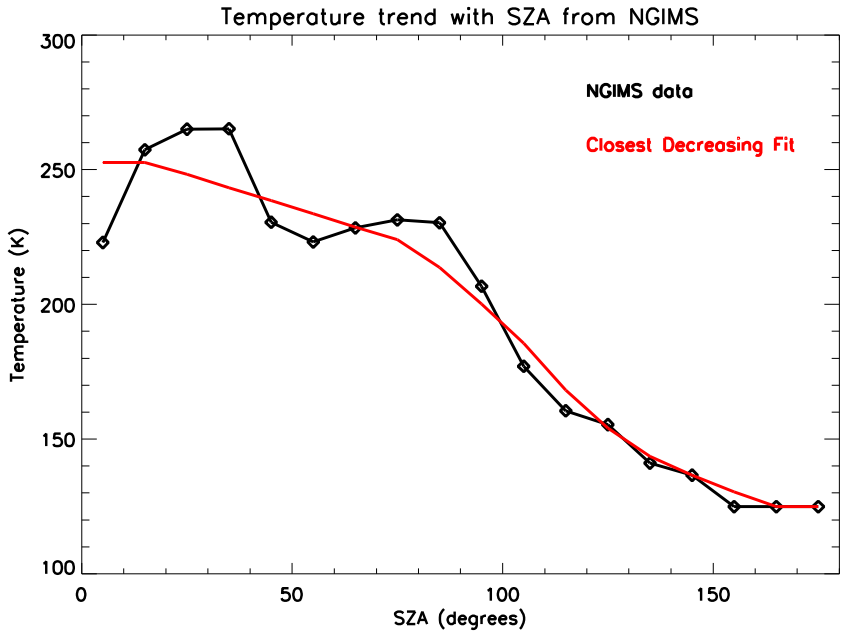


Figure 1: *Exobase temperature trend with solar zenith angle determined from analysis of NGIMS observations of the martian atmosphere. The black line depicts measurements made by MAVEN – NGIMS whereas the red line is the closest decreasing fit to the data.*

The exobase temperature at SZA = 0˚ for thermal H and D at Mars for a particular solar longitude (L_s) along Mars' orbit is pre-determined by fitting the MAVEN-NGIMS derived temperatures for the lower thermosphere at perihelion and aphelion with a sine wave given by

$$y(L_s) = A\,Sin\left(\frac{(L_s - 1.239}{2}\ radians\right) + B \quad (1)$$

In the above equation y represents the temperature at SZA = 0˚ for a particular L_s, A is the difference between the aphelion and perihelion derived NGIMS temperatures at SZA = 0˚ and B is the aphelion temperature at SZA = 0˚. NGIMS observations at aphelion and perihelion included a large sample of measurements covering solar zenith angles from ~50° to 110° at aphelion and ~5° - 140° at perihelion. This data was used to constrain the exobase temperature at SZA = 0˚ by extrapolating the temperature curve of Figure 1 as well as shifting it up/down to match the derived temperatures at their corresponding solar zenith angles for aphelion and perihelion.

Mars' thermospheric temperatures at aphelion and perihelion were determined using NGIMS observations of CO_2 and Ar densities at MAVEN's periapsis altitudes (~150-180 km). The slope of the CO_2 and Ar density measurements between 160 – 220 km were used to derive the atmospheric scale height, and thereby the temperature of the background atmosphere. Since the difference in the derived temperature values from the scale heights of CO_2 and Ar were within the measurement uncertainties, the values were averaged to determine the martian thermospheric temperature at aphelion and perihelion for the available solar zenith angles. The temperature curve represented in Fig. 1 was then utilized to approximate the exobase temperature at the sub-solar point [Mayyasi et al., 2019]. The resulting aphelion and perihelion temperatures at the exobase altitude of 200 km and SZA = 0° for Mars were determined to be 216 ± 39 K and 255 ± 29 K respectively [Mayyasi et al., 2019]. These temperatures are only representative of exospheric populations of D and H that are in thermal equilibrium with the bulk atmosphere (i.e. CO_2) below the exobase. Temperature of non-thermal D and H cannot be estimated using this method.

The temperature variations with altitude were determined from the analytical expression of Krasnopolsky [2002]. At present this is the only existing analytical expression for determining temperature variation with altitude and was established using Viking 1's measurement of neutral densities (CO_2, N_2, CO, O_2 and NO) at Mars between 120-200 km. This functional form was modified to include a SZA dependence and is written as:

$$T(z, sza) = T_\infty(sza) - (T_\infty(sza) - 125)e^{-\frac{(z-90)^2}{11.4T_\infty(sza)}} \quad (2)$$

T_∞ here represents a temperature at a reference altitude of 300 km, and is taken to be slightly higher than the pre-determined temperature at the exobase altitude (200 km) such that the temperature curve derived using eq. (2) intersects the known exobase temperature value. The variable z in the equation represents an altitude range of 80 – 200 km. Beyond 200 km the temperature assumes the value of the exobase temperature for a particular SZA. Figure 2 shows the temperature curves derived for a solar longitude of 74° and 251.6° for Mars for a non-isothermal atmosphere.

2.2 Variation of Deuterium and Hydrogen density with SZA, solar longitude and altitude

The variation of density with SZA for both D and H is calculated by using the Hodges and Johnson [1968] formulation for light species, where the species density at the exobase is determined to be a function of only the exobase temperature and is given by the relation,

$$n\,T^{5/2} = constant \quad (3)$$

In the above equation n represents the exobase density of the species and T represents the exobase temperature of the species at a particular SZA. This relationship holds true for hydrogen because H density near the exobase adjusts with local temperature changes such that the net local upward ballistic flux is balanced by the net local downward ballistic flux. There is no influx of additional H atoms into the exosphere as the ballistic transport timescale is shorter than the vertical diffusion timescale of H into the exosphere through the lower atmosphere. This was confirmed through Mars Global Circulation Model (MGCM) simulations for hydrogen [Chaufray et al., 2018]. In the modeling process presented here, it was assumed that deuterium, the heavier isotope of hydrogen, also obeys this relationship.

The density profile with altitude for D and H calculated at Mars extends from 80 km to 50,000 km in the model. The process of constructing the density profile with altitude involves three different approaches applied to three different altitude ranges.

2.2.1 *Above the exobase: 200 – 50,000 km*

The region above the exobase is considered to be almost collisionless. In a 1-D situation, where the exosphere is considered to be spherically symmetric and isothermal, the Chamberlain approximation [Chamberlain, 1963] works well for different planetary bodies. Chamberlain's theory makes the assumption that the exospheric atoms at the exobase level obey the Maxwell-Boltzmann velocity distribution with a single mean temperature, which is the exobase temperature. However, in the case of a non-spherically symmetric and non-isothermal atmosphere a classical Chamberlain approach is not applicable. In order to simulate exospheric densities for an asymmetric atmosphere, the approach developed by Vidal-Madjar and Bertaux [1972] was adopted here. Under this approach, the exosphere is considered to be made up of populations of particles which obey the Maxwell-Boltzmann velocity distribution with different mean temperatures corresponding to different launch points on the exobase. The particle distribution function has a Maxwellian form that depends on the velocity (V_c), the longitude (α_c) and the latitude (δ_c) at the critical altitude, i.e. the exobase of Mars and has the form given by:

$$f_c(\alpha_c, \delta_c, V_c) = N_c(\alpha_c, \delta_c) \left[\frac{1}{2\pi m k_b T_c(\alpha_c,\delta_c)}\right]^{3/2} exp\left[\frac{-mMGV_c^2}{r_c\, k_b\, T_c(\alpha_c,\delta_c)}\right] \quad (4)$$

Here $N_c(\alpha_c, \delta_c)$ is the number density at the exobase as a function of the longitude and latitude, m the mass of the species, k_b the Boltzmann's constant, $T_c(\alpha_c, \delta_c)$ the exobase temperature which is also a function of longitude and the latitude, r_c the exobase altitude (200 km for Mars), V_c the velocity at the exobase normalized to the escape velocity, M the mass of the planet and G the universal gravitational constant. The number density at any point in space is written as:

$$N_c(y, \alpha_c, \delta_c) = \int f_c\, d^3p_i \quad (5)$$

The above integral is over the total population that occupies an element of momentum space (d^3p_i) and is restricted to existing trajectories of particles (ballistic, satellite and escaping trajectories) that may occupy the momentum space. The subscript i represents the i^{th} particle (i = 1,2,…n). Satellite trajectories are neglected in the model. Appendix A details the Vidal-Madjar and Bertaux [1972] approach used in this study.

2.2.2 *From the homopause to the exobase: 120 – 200 km*

315 The homopause altitude for the martian atmosphere is taken to be at ~120 km in the model
316 [Krasnopolsky et al., 1998; Nagy et al., 2009; Mahaffy et al., 2015c]. Therefore, the region
317 between 120 – 200 km has the different species diffusively separated in the atmosphere of Mars.
318 Since CO_2 is by far the most dominant species at these altitudes, the modeling process considers
319 only the diffusion of either D or H in CO_2 at these altitudes and utilizes a very simple diffusion
320 model [Chaufray et al., 2008; Bhattacharyya et al., 2017a] to derive the density of D or H in this
321 region of the martian atmosphere. However, for the asymmetric, non-isothermal atmosphere the
322 diffusion equation for deriving deuterium or hydrogen densities is applied at every SZA since the
323 temperature profile with altitude varies with SZA. The CO_2 profile is derived by applying the
324 equation of hydrostatic equilibrium at every SZA for a given temperature structure starting from
325 the lower boundary of the atmosphere (80 km). The CO_2 density at 80 km was determined using a
326 neutral atmosphere model which utilized a volume mixing ratio at 80 km, consistent with the
327 relative abundances for CO_2 found in the Mars Climate Database for the temperature profile
328 derived from NGIMS measurements as described in section 2.1 [Forget et al., 1999; Lewis et al.,
329 1999]. The model also accounted for molecular and eddy diffusion for interactions of CO_2
330 molecules with other neutral species in the martian atmosphere in order to obtain the CO_2 density
331 at 80 km [Matta et al, 2013; Mayyasi et al., 2019]. This modeling procedure was only applied at
332 aphelion and perihelion where the exobase temperature and its variation with SZA had been well
333 established through NGIMS observations. At any other solar longitude, the CO_2 density at 80 km
334 was determined through sinusoidal interpolation of the CO_2 densities derived at the aphelion (L_s =
335 71˚) and perihelion (L_s = 251˚) position of Mars' orbit using eq. (1) where the variables y, A and
336 B now refer to CO_2 density. The CO_2 density at the lower boundary is kept a constant and is not
337 varied with SZA in the model as the CO_2 mixing ratios at 80 km used in the model did not show
338 significant variability with SZA. However, using the mixing ratios in the neutral atmosphere model
339 did not account for atmospheric variability introduced by pressure differences. Thus, the modeled
340 CO_2 density profile with altitude obtained from the hydrostatic equilibrium assumption only varies
341 with SZA due to differences in the temperature profile. The CO_2 density at 80 km was determined
342 to be 9.16×10^{12} cm^{-3} at aphelion and 2.29×10^{13} cm^{-3} at perihelion. Appendix B summarizes the
343 equations applied to this region of the atmosphere in order to derive the density distribution of D
344 or H.

345 *2.2.3 From the model base to the homopause: 80 – 120 km*

At altitudes of 80 – 120 km, the martian atmosphere is well-mixed. In this region, the deuterium/hydrogen density distribution was assumed to decrease exponentially with increasing altitude constrained by the boundary values at 80 and 120 km. The density at 120 km is estimated through the simple diffusion model (Section 2.2.2). For hydrogen, the starting density at 80 km is determined by multiplying the H exobase density, which is a free parameter in the model, by a ratio (density of hydrogen at 80 km to the exobase density of hydrogen). This ratio is calculated from the density profile derived for H at aphelion and perihelion between 80 to 300 km using MAVEN-NGIMS derived temperature profile (section 2.1) in conjunction with the same neutral atmosphere model which was used to derive the CO_2 density at 80 km. The model accounts for hydrogen chemistry in the martian atmosphere and utilized a volume mixing ratio for H at 80 km from the Mars Climate Database in order to derive the hydrogen density profile with altitude at aphelion and perihelion [Matta et al., 2013]. For all other solar longitudes, the value of this ratio is determined by sinusoidally interpolating between the aphelion and the perihelion value using eq. (1). This ratio, calculated for hydrogen, is assumed to be the same for deuterium in order to satisfy the D/H ratio constraint at Mars. For aphelion, the value of the ratio is determined to be ~25 whereas at perihelion the ratio has a value of ~58. Like CO_2, the densities of H and D at 80 km are kept constant and do not have any SZA dependence.

Figure 2 shows an example of modeled deuterium and hydrogen density profile at $L_s = 74°$ and $L_s = 251.6°$ as well as the corresponding temperature and CO_2 density profile and their variation with solar zenith angle. This density profile for D and H was generated for an arbitrary exobase density of 1×10^3 cm^{-3} for D and 1×10^5 cm^{-3} for H at SZA = 0°. This value of exobase density for D or H is the only free parameter in the atmosphere model.

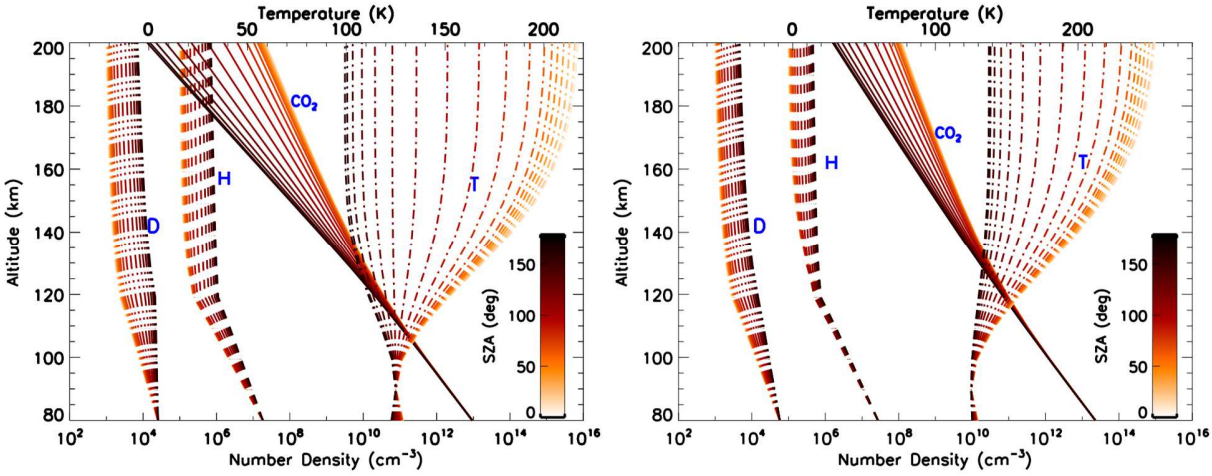


Figure 2: *Variation of temperature, CO_2 density, hydrogen density and deuterium density with altitude and solar zenith angle at a solar longitude L_s = 74° (left), which is close to aphelion and L_s = 251.6° (right), which is close to perihelion, derived using the two-dimensional density model. As is evident from the figure, there is significant variation in the different species density and temperature between the sub-solar and the anti-solar point in the atmosphere of Mars.*

3. Calculating the line of sight intensity of D and H at Lyman α

The solar Lyman α photons undergo resonant scattering both by the deuterium and the hydrogen atoms in the exosphere of Mars. However, the deuterium densities at the martian exobase are orders of magnitude lower than hydrogen exobase densities. Therefore, the solar Lyman α photons at 1215.33 Å undergo only single scattering by deuterium atoms at Mars, because of which the line of sight Lyman α intensity recorded at 1215.33 Å is directly proportional to the column density of deuterium. This makes it easier to translate the observed intensities into density distributions for deuterium in the exosphere of Mars. For hydrogen, the larger densities in comparison to deuterium results in multiple scattering of the Lyman α photons at 1215.67 Å, because of which observed line of sight intensities cannot be directly translated into column densities. Rigorous radiative transfer modeling is required to interpret the observed intensities in order to derive a density distribution for hydrogen. The following sections describe the method by which the deuterium and hydrogen Lyman α intensities were calculated for a given density distribution, which can then be used to simulate Mars D and H Lyman α observations.

3.1 Determining the deuterium Lyman α intensity at 1215.33 Å

For a given deuterium density distribution generated using the two-dimensional atmosphere model (Section 2), the intensity along any line of sight passing through the atmosphere was determined by calculating the column density along that line of sight and multiplying it by the Lyman α excitation frequency at 1215.33 Å (g-value) at Mars. The excitation frequency can be calculated using the following relation:

$$g = F_0 \times \sigma_0 \times \Delta\lambda_D \times \sqrt{\pi} \quad (6)$$

In the above equation g is the excitation frequency in s^{-1}, F_0 the Lyman α line center flux at Mars (photons/cm^2/s/Å), σ_0 the Lyman α scattering cross section (cm^2) of deuterium at 1215.33 Å and

$\Delta\lambda_D$ the Doppler width of the Mars line (Å). The value of g is independent of the gas temperature as the temperature dependence of the scattering cross section and the temperature dependence of the Doppler width term cancel each other out.

3. 2 Determining the hydrogen Lyman α intensity at 1215.67 Å

The solar Lyman α photons at 1215.67 Å undergo multiple scattering in the hydrogen exosphere of Mars. Therefore, a radiative transfer model is required to analyze the optically thick hydrogen Lyman α emissions from the martian exosphere. Earlier modeling efforts were restricted to a spherically symmetric and isothermal atmosphere [Anderson and Hord, 1971; Anderson 1974; Chaufray et al., 2008; Chaffin et al., 2014; 2015; 2018; Bhattacharyya et al., 2015; 2017a; 2017b]. From MAVEN and HST observations, it became evident that the hydrogen exosphere is unlikely to be spherically symmetric and isothermal [Chaffin et al., 2015; Bhattacharyya et al., 2017a]. The MAVEN observations found a ~100 K difference in temperature between the sub-solar and anti-solar region of the atmosphere [Figure 1; Stone et al., 2018; Mayyasi et al., 2019]. Therefore, a two-dimensional radiative transfer model was developed in order to simulate multiple scattering in a non-spherically symmetric, and non-isothermal atmosphere, which was then used to analyze the MAVEN and HST observations of H Lyman α emission from Mars. Appendix B describes the 2-D radiative transfer model in detail. The Lyman α scattering frequency at 1215.67 Å is calculated using equation 6. Once the single and multiple scattering source functions have been determined from the 2-D radiative transfer model for a given atmosphere, the line of sight H Lyman α intensity can be derived using the following equation:

$$I_\vartheta(r,\theta,\varphi) = I_\vartheta(r_\infty,\theta,\varphi)e^{-\tau_\vartheta(r,r_\infty)} + \int_r^{r_\infty} S_\vartheta\,(r,\theta,\varphi)\,e^{-\tau_\vartheta(r,r')}\,ds' \quad (7)$$

In the above equation which describes the intensity along a line of sight passing through the martian atmosphere, r, θ, and φ are the three coordinates in the spherical coordinate system, $I_\vartheta(r_\infty,\theta,\varphi)$ is the Lyman α intensity contribution from external sources like the interplanetary hydrogen medium (IPH) or the geocorona, $e^{-\tau_\vartheta(r,r')}$ the total extinction of the Lyman α photons along the line of sight due to absorption by CO_2 as well as scattering by H atoms present in the martian atmosphere and $S_\vartheta\,(r,\theta,\varphi)$ the total source function or the volume emission rate at a particular point in the martian atmosphere due to single and multiple scattering of solar Lyman α photons. Lyman α intensity due to external sources when present is subtracted off from the data

either using observations or models for those external sources. For the MAVEN-IUVS limb observations, the external source was IPH which was estimated using the Pryor model [Pryor et al., 1992; 2013; Ajello et al., 1987] and subtracted off from the martian hydrogen Lyman α emission. For the HST observations, a dedicated orbit for every Mars observing visit observed the blank sky in order to capture the background emission from the IPH and the geocorona. Data from this orbit was used to remove the background Lyman α emissions present in the Mars observations.

4. Modeling D and H Lyman α observations with HST and MAVEN

Both the deuterium and the hydrogen Lyman α emissions at Mars have been extensively observed with MAVEN and the hydrogen Lyman α emission with HST and MEX [Clarke et al., 2014; 2017; Chaffin et al., 2014; 2015; 2018; Bhattacharyya et al., 2015; 2017a; 2017b; Mayyasi et al., 2017b; 2018; 2019; Chaufray et al., 2008]. These observations have been analyzed with the goal of constraining the present-day H and D escape rates, which are direct tracers of water and bulk atmospheric escape from Mars throughout its evolution history. While determining the H escape flux using HST observations, it was noted that several factors increase the uncertainty in the derived H escape flux values [Bhattacharyya et al., 2017a]. Among them are the absolute calibration of the instrument and the assumption of a spherically symmetric and isothermal exosphere in modeling Mars. This section presents an improved absolute calibration for HST and compares it with MAVEN, as well as presents a comparison of the symmetric vs. asymmetric model fits to the data.

4.1 Absolute Calibration of HST and comparison with MAVEN

The Hubble Space Telescope has been used extensively to study the hydrogen exosphere of Mars [Clarke et al., 2014; Bhattacharyya et al., 2015; 2017a; 2017b]. Far ultraviolet images of the Lyman α emission from the martian exosphere have been obtained using the Advanced Camera for Surveys (ACS) instrument on HST. These images were analyzed to infer the hydrogen escape rates from the exosphere of Mars. However, the ACS images were obtained by using broadband filters and therefore the exact sensitivity of the detector at Lyman α is unknown. This increased the uncertainty in the derived hydrogen escape flux upon analysis of the data.

More recently, an HST observing campaign was conducted with the sole purpose of calibrating the ACS detector at Lyman α (1215.67 Å). This calibration campaign utilized the

Space Telescope Imaging Spectrograph (STIS) instrument whose sensitivity has been well calibrated at the Lyman α wavelength. The STIS instrument was used to observe the geocoronal Lyman α emission for one HST orbit. The same patch of sky was then observed by the ACS instrument through the next HST orbit. The geocoronal Lyman α intensities recorded by the two instruments were then compared against each other to derive the absolute calibration of ACS at Lyman α. The new calibration factor for ACS at Lyman α is 0.001935 counts pixel^{-1} sec^{-1} kR^{-1}. This value is 36% smaller than the older theoretically calculated value of 0.002633 counts pixel^{-1} sec^{-1} kR^{-1}. Figure 3a shows the comparison between the STIS and the ACS recorded intensities of the geocorona using the old calibration factor derived theoretically (0.002633 counts pixel^{-1} sec^{-1} kR^{-1}) [Bhattacharyya et al., 2017a] and the new calibration factor of 0.001935 counts pixel^{-1} sec^{-1} kR^{-1} derived through the HST ACS calibration campaign.

The new calibration factor derived for ACS was tested by comparing overlapping observations of the martian hydrogen Lyman α emission obtained using STIS and ACS on 12th November 2014 and 3rd December 2015. Figure 3b shows the comparison between the STIS and the ACS intensity of the martian exosphere at 1215.67 Å. The two profiles lie on top of each other for both the observing visits thereby validating the new ACS calibration factor.

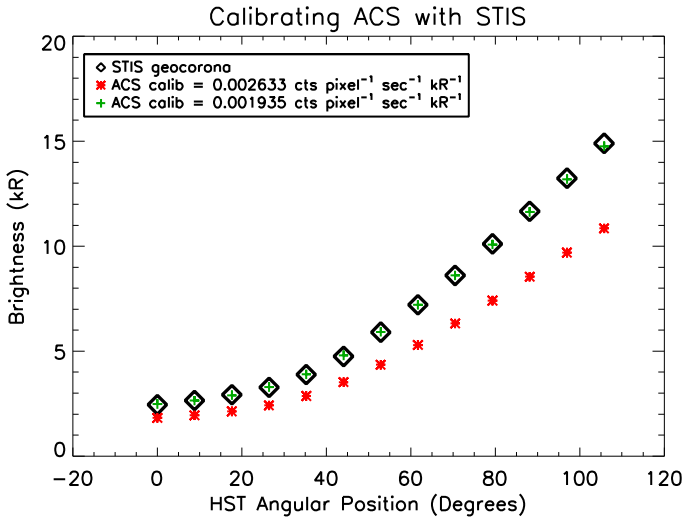


Figure 3a: *This figure shows the geocoronal intensities observed by the STIS instrument as well as the ACS instrument onboard HST when observing the same patch of the sky with HST's orbital position in degrees. The ACS intensities processed using the old calibration factor (0.002633*

counts pixel^{-1} sec^{-1} kR^{-1}) do not match up well with the STIS intensities, whereas, with the new calibration factor the values recorded by the two instruments overlap completely.

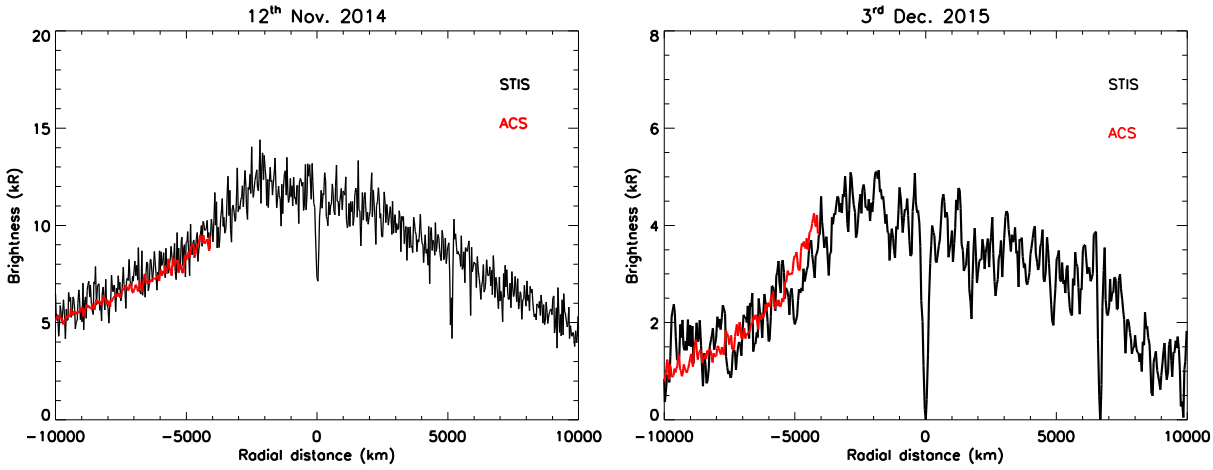


Figure 3b: *The above two figures show the brightness of Mars' Lyman α emission (with the geocoronal + interplanetary hydrogen background subtracted) as observed by STIS (black) and ACS (red) on 12th November, 2014 and 3rd December, 2015. The new calibration factor derived for ACS was used to determine the brightness of the martian hydrogen exosphere as observed by ACS for the above two observations. As can be seen in the two figures, the ACS intensities match those measured by STIS, i.e. the red line (ACS intensity) overlaps with the black line (STIS intensity) for both observations.*

Comparison of HST-ACS observed brightness for the martian exosphere with MAVEN is not a straightforward process. The two instruments have different observing geometry and lines of sight. The ACS brightness values have to be analyzed and fit to models to obtain the hydrogen density distribution in the martian exosphere that best matches the data for a particular day of observation. Using this density distribution, the modeled HST brightness for MAVEN-IUVS observing geometry can then be derived and compared with the actual brightness recorded by the MAVEN satellite in orbit around Mars on the same observation date. This comparison study was conducted for two specific dates, 12th November 2014 and 3rd December 2015 where there were corresponding dayside observations available with both HST and MAVEN. For the comparison study, only disk observations of Mars by the MAVEN-IUVS echelle were used in order to avoid uncertainties in the modeling process brought on by the presence of interplanetary hydrogen background in the MAVEN-IUVS signal. Figure 4 shows the comparison between the model

derived brightness that would be observed by HST (red points) in MAVEN's observing geometry with the actual brightness observed by MAVEN-IUVS echelle (black points). The brightness derived from modeling the HST observations and the actual brightness observed by MAVEN are within the uncertainty. There is an offset between HST and MAVEN intensities for the 2015 observations which could be due to an inaccurate derivation of Mars' exospheric characteristics from the HST observations because of larger noise in the data (Figure 7) as a result of low count rate since Mars was close aphelion during the 2015 observation with the solar activity approaching minimum. However, the MAVEN IUVS observational intensities for 3rd December 2015 do fall within the 10% uncertainty accorded to the model results.

A similar comparison study was presented in Mayyasi et al. [2017a] for the 12th November 2014 overlapping observations with MAVEN-IUVS echelle and HST. However, the HST observations were reduced using the old calibration factor for ACS and the modeling was done using a 1-dimensional radiative transfer model for observed H Lyman α intensities. The resulting comparison with MAVEN was not as accurate as the figure below [figure 4 left].

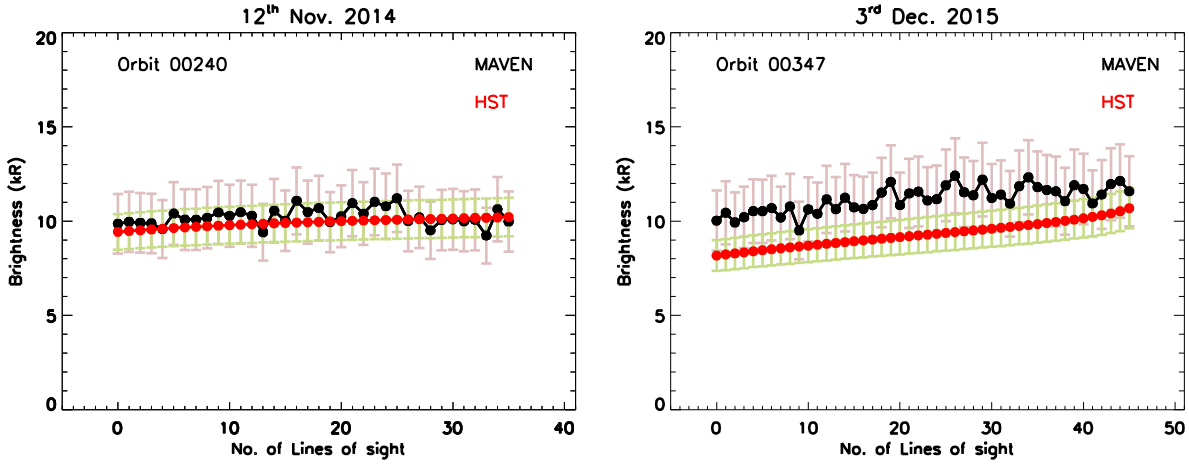


Figure 4: *Comparison between the model derived Mars disk brightness that would be observed by HST (red points) in MAVEN-IUVS echelle observing geometry with the actual brightness observed by MAVEN-IUVS Echelle (black points) on 12th November 2014 and 3rd December 2015. The uncertainty in the brightness observed by MAVEN due to the ~25% uncertainty in absolute calibration is represented by the light pink lines whereas the light green lines represent the uncertainty in the model derived brightness which is taken to be ~10%.*

4.2 Modeling MAVEN and HST observations using an asymmetric atmosphere

MAVEN observations of H and D Lyman α as well as HST observations of H Lyman α were modeled using an asymmetric atmosphere and the 2-D radiative transfer model as described in sections 2 and 3 respectively. The MAVEN observations with the IUVS-echelle instrument are restricted to lower tangent altitude ranges between 0 – 300 km, whereas the HST observations extend from 700 – 30,000 km. The hydrogen exosphere at Mars approaches a more uniform and spherically symmetric structure above ~2.5 martian radii [Holmström, 2006; Bhattacharyya et al., 2017a]. Therefore, the 2-D model is more important for an accurate analysis and interpretation of the MAVEN IUVS-echelle observations of the martian H Lyman α emission.

4.2.1. Modeling MAVEN IUVS-Echelle Observations of Deuterium

MAVEN IUVS-Echelle observations of D Lyman α between November 2014 – October 2017 have been analyzed using the 2-D asymmetric model in order to derive best-fit exobase densities for D (2952 orbits in total), the results of which have been published in Mayyasi et al. [2019]. These observations have also been previously used to study the seasonal variability of the deuterium Lyman α intensity in the martian exosphere [Clarke et al., 2017; Mayyasi et al., 2017]. In this paper, a detailed description of the modeling process supporting the data analysis is presented.

For modeling the MAVEN IUVS-Echelle observations of D, first the exobase temperatures are pre-determined by interpolating NGIMS observations at aphelion and perihelion for all the MAVEN-IUVS echelle orbits (section 2.1). Then the 2-D atmosphere model was used to produce density distributions for a total of 7 different exobase densities, 100, 500, 1000, 3000, 5000, and 7000 cm^{-3} at SZA of 0° for every MAVEN IUVS echelle orbit (2952 × 7 = 20664 atmospheres simulated). For each model atmosphere corresponding to a particular MAVEN IUVS echelle orbit, the line of sight deuterium Lyman α intensity was calculated by deriving the column density along that line of sight and multiplying it by the excitation frequency of Lyman α at 1215.33 Å (eq.6).

The line integrated solar Lyman α at 1215.67 Å flux is measured by the Extreme Ultraviolet Monitor (EUVM) instrument onboard the MAVEN orbiter at Mars [Eparvier et al., 2015]. It has a full width half max (FWHM) of 1 Å and therefore encompasses the solar Lyman α flux at 1215.33 Å. From the EUVM measurements of the line integrated flux, the Lyman α flux at line center (1215.67 Å) was calculated by using the widely-used Emerich relationship [Emerich et al., 2005]. Based on the shape of the Lyman α profile, the solar Lyman α flux at 1215.33 Å is derived, which

549 is almost the same as the flux at line center (greater by ~1.6%), and this value is used in determining
550 the excitation frequency of Lyman α at 1215.33 Å for all the MAVEN-IUVS echelle orbits.

551 Since the deuterium signal is faint at Mars, the data was binned into L_s, SZA and altitude bins
552 to obtain intensity profiles with altitude for deuterium. Six L_s bins were created with 20° spacing
553 within solar longitudes 220° - 340°, four SZA bins were created between 30° - 90° with 15° spacing
554 and twenty one altitude bins were created between 0 – 400 km with 20 km spacing as elaborated
555 in Mayyasi et al., [2019]. The model followed the same binning scheme as the data using the 2952
556 orbits to produce simulated intensity profiles with altitude which can then be compared to the data.
557 These modeled intensity profiles derived for the seven different exobase densities were then
558 linearly interpolated on a more refined exospheric density grid to obtain the best fit exospheric
559 density of deuterium that matched the data through the process of χ^2 minimization.

560 Figure 5 shows the comparison between the best fit modeled density to the data for deuterium
561 as measured by IUVS echelle using the spherically symmetric model, which assumes an isothermal
562 symmetric atmosphere [Bhattacharyya et al., 2017a], and the spherically asymmetric model
563 described here. The figure shows four cases for available dayside solar zenith angles for the
564 northern hemisphere (top two plots) and the southern hemisphere (bottom two plots) as observed
565 by the IUVS echelle instrument onboard MAVEN [Mayyasi et al., 2019]. In all cases the
566 asymmetric model fits the data better than the symmetric model for the exobase density displayed
567 in the respective figures. However, even the asymmetric model fails to provide perfect fits to the
568 data, especially at lower altitudes. This is because the D signal is above the detection threshold of
569 the MAVEN-IUVS detector only between L_s = 220° - 340° and the dataset presented in figure 5,
570 which was analyzed and reported in Mayyasi et al. [2019], has dayside coverage of that solar
571 longitude range only during late 2014 – early 2015. During this time MAVEN had just started its
572 science phase and the optimal conditions like detector gain, binning scheme, observing geometry,
573 etc. for recording the D emission from the martian exosphere had not yet been established, thereby
574 degrading the quality of the data collected. It is expected that more IUVS observations of the D
575 emissions through multiple perihelion passages of Mars in the future would provide better model
576 fits to the data.

577 An advantage of the asymmetric model is that it allows analysis and comparison of IUVS
578 observations at different solar zenith angles under the same solar longitude and solar activity
579 conditions using a single model run in order to better constrain the asymmetric nature of Mars'

exosphere. Presently, this has not been possible for D due to the lack of observations [Mayyasi et al., 2019]. But with IUVS's continued observations of the D Lyman α emission with every perihelion passage of Mars, this would soon be possible.

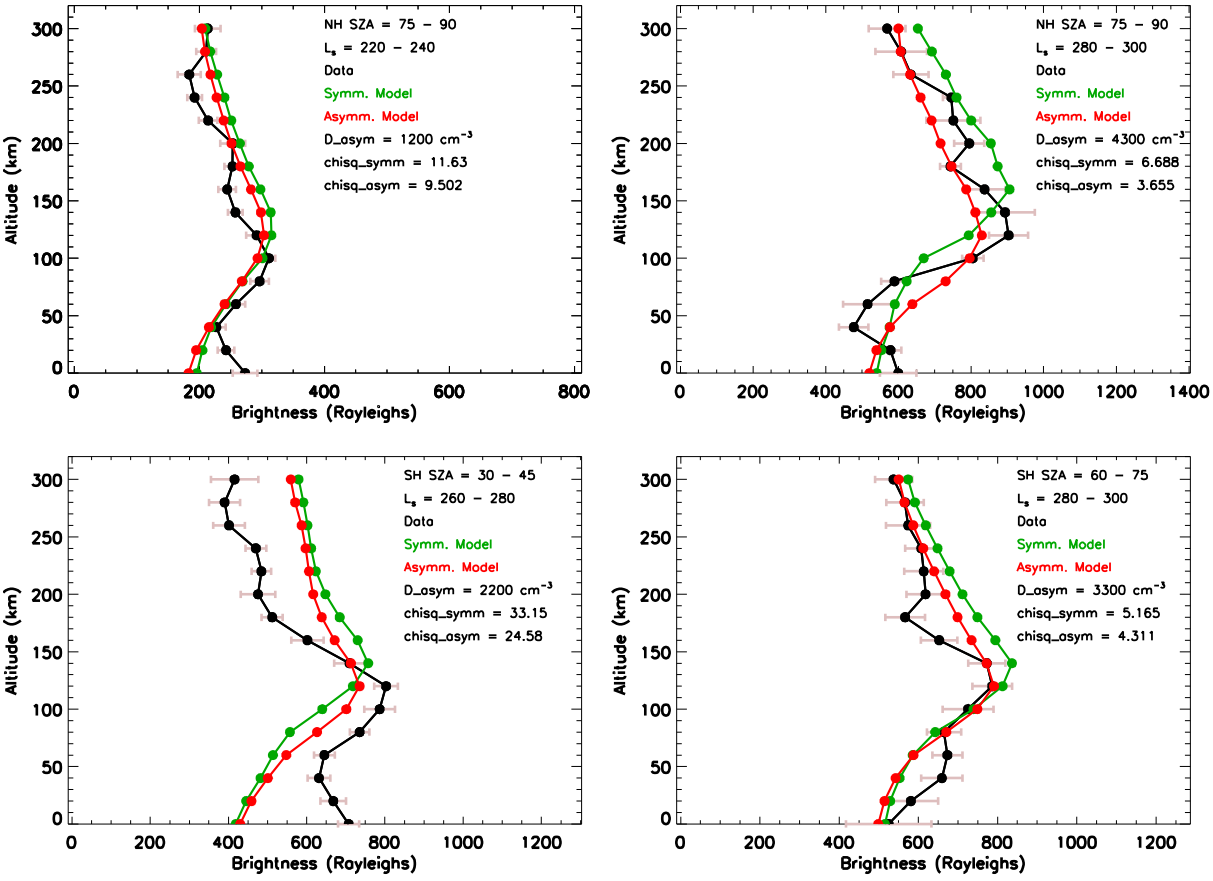


Figure 5: *This figure displays the symmetric and asymmetric model fits to the IUVS-Echelle deuterium observation for a predetermined exobase temperature from MAVEN-NGIMS observations and an exobase density at SZA = 0° as displayed in the figures. The exobase density varied with SZA following the Hodges and Johnson [1968] formulation for the asymmetric model, but remained constant for the symmetric model. The top two plots are for the northern hemisphere and the bottom two plots are for the southern hemisphere. These simulations are for an MAVEN-NGIMS measured aphelion temperature of 216 K and a perihelion temperature of 255 K [Mayyasi et al., 2019].*

4.2.2. Modeling MAVEN IUVS-Echelle Observations of Hydrogen

MAVEN observations of H Lyman α between November 2014 – October 2017, simultaneously observed with the D Lyman α emission by the IUVS echelle instrument, have been utilized in this study (2952 orbits in total). Some of the observations have been previously used to study the seasonal variability of hydrogen in the martian exosphere as well as the response of the H escape rate to solar flare events [Clarke et al., 2017; Mayyasi et al., 2018]. For modeling the MAVEN observations of hydrogen, the 2-D radiative transfer model (Appendix B) in conjunction with the 2-D atmosphere model (section 2; Appendix A) was used to determine the emissivity for a range of exobase densities for thermal hydrogen ($10^4 - 7 \times 10^5$ cm^{-3}; 13 different exobase density values) at Mars' aphelion and perihelion positions (26 simulations with the 2-D atmosphere + RT model). The exobase temperatures at perihelion and aphelion positions were pre-determined by averaging NGIMS observations of the lower thermosphere conducted over a period of ~1.5 Mars years (section 2). The emissivity of Mars' atmosphere for all the MAVEN-IUVS echelle orbits (2952 orbits in total) for each exobase was calculated by sinusoidally interpolating the emissivity determined at aphelion and perihelion using the 2-D RT model using eq. 1. The Lyman α line center flux at 1215.67 Å in the model was determined from EUVM measurements of the line integrated flux which were then converted to line center flux using Emerich's analytical formula [Emerich et al., 2005]. Next, the line of sight hydrogen Lyman α intensity for each MAVEN-IUVS echelle orbit was calculated using equation 7. The model results were then binned into solar longitudes, SZA and altitude bins, same as the deuterium observations to facilitate D/H calculations which will be published in a future study. This modeled and observed intensity profiles were compared and the density that best matched the data was determined through the process of χ^2 minimization. Non-thermal hydrogen was not considered in the modeling process because the altitude profiles are restricted to line of sight altitudes below ~3000 km, where the thermal component is dominant.

Figure 6 shows the comparison between MAVEN IUVS echelle measurements of H Lyman α emission and the best modeled fit to the data using the asymmetric model and the symmetric model. This figure displays the corresponding H Lyman α emission to the D Lyman α emission measured by the IUVS echelle instrument displayed in figure 5. The error bars are larger for the fainter D Lyman α emission than for the much brighter and easily detectable H Lyman α emission. Unlike the D observations, the H Lyman α observations above the limb include a contribution from the interplanetary hydrogen (IPH). The IPH intensity was estimated using the widely used Pryor

model [Pryor et al., 1992; 2013; Ajello et al., 1987]. As is evident from the figure, the asymmetric model provides a better fit to the data than the symmetric model for the exobase density displayed in the respective figures.

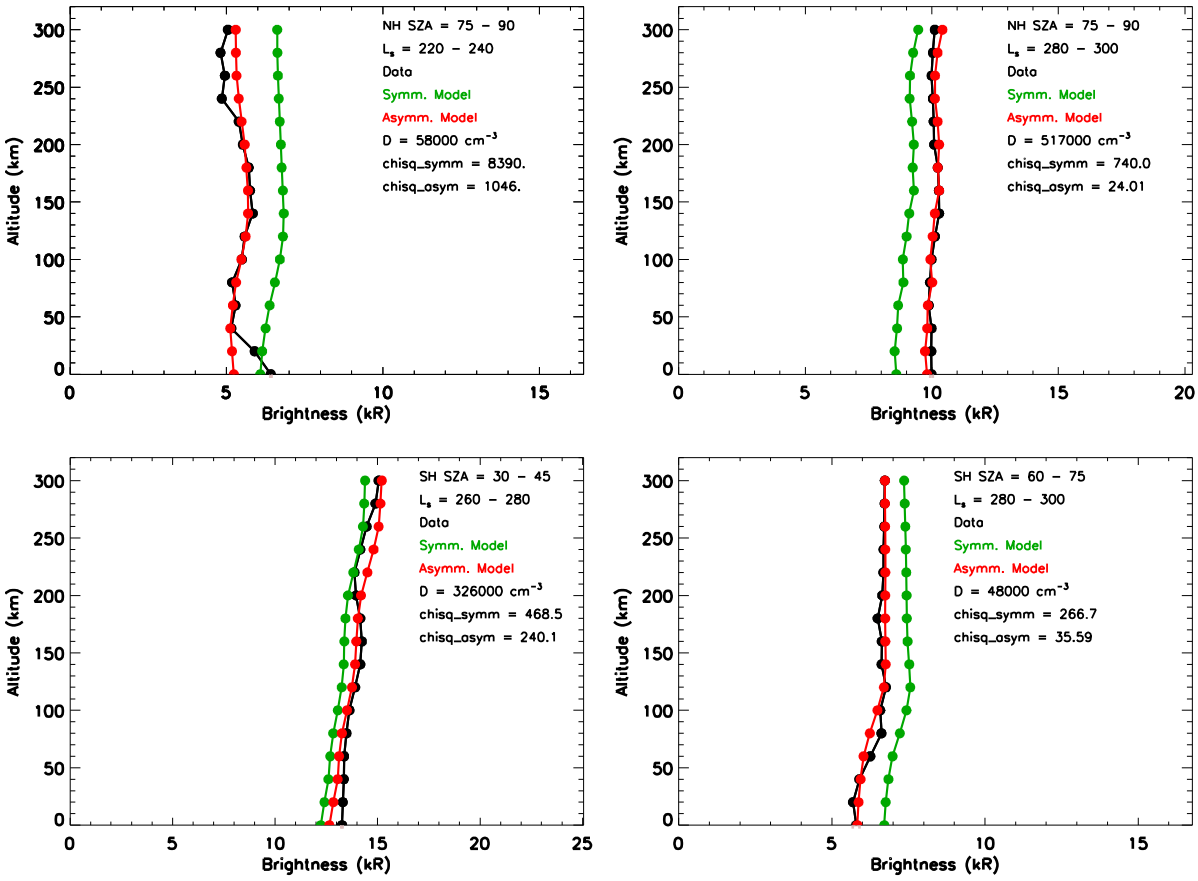


Figure 6: *This figure displays the symmetric and asymmetric model fits to the IUVS-Echelle hydrogen observations for a predetermined exobase temperature from MAVEN-NGIMS observations and an exobase density at SZA = 0° as displayed in the figures. The exobase density varied with SZA following the Hodges and Johnson [1968] formulation for the asymmetric model, but remained constant for the symmetric model. The top two plots are for the northern hemisphere and the bottom two plots are for the southern hemisphere. These simulations are for an MAVEN-NGIMS measured aphelion temperature of 216 K and a perihelion temperature of 255 K [Mayyasi et al., 2019].*

4.2.3. Modeling HST Observations of Hydrogen

Two sets of HST observations obtained on 12th November 2014 and 3rd December 2015 were modeled using the 2-D atmosphere + radiative transfer model as well as the 1-D atmosphere + radiative transfer model and the comparison between the two model results were studied. On the above-mentioned observation dates, Mars was imaged using two different instruments on the HST, i.e., ACS and STIS. The ACS instrument was used to image the highly extended dayside hydrogen exosphere of Mars. The ACS images for the martian Lyman α emission are a difference between two images obtained with the F115LP filter, which transmits Lyman α, and the F140LP filter, which blocks Lyman α but allows emissions up to 140 nm wavelengths. Therefore, the disk of Mars in the final differenced image is noisy on account of other emissions like oxygen 130.4 nm and the 135.6 nm emissions and solar continuum. However, above ~700 km the hydrogen Lyman α emission becomes dominant. Therefore, the ACS observations capture the Mars H Lyman α profile accurately above ~700 km. The STIS observations, on the other hand, can spectrally isolate the Lyman α emission from the Mars disk. Thus, both ACS and STIS observations of Mars were combined together to obtain the martian H Lyman α intensity profile from the dayside to the night side including the disk. Background emissions from the interplanetary hydrogen (IPH) and the geocorona in the Mars observations were estimated using a dedicated HST orbit as a part of each visit which observed the background blank sky 5 arcminutes away from Mars for the same portion of HST's orbit as the Mars observations with STIS and ACS. The estimated background intensity was then subtracted off from the Mars H Lyman α data. Figure 7 shows the final Mars H Lyman α profile obtained for the two observation days.

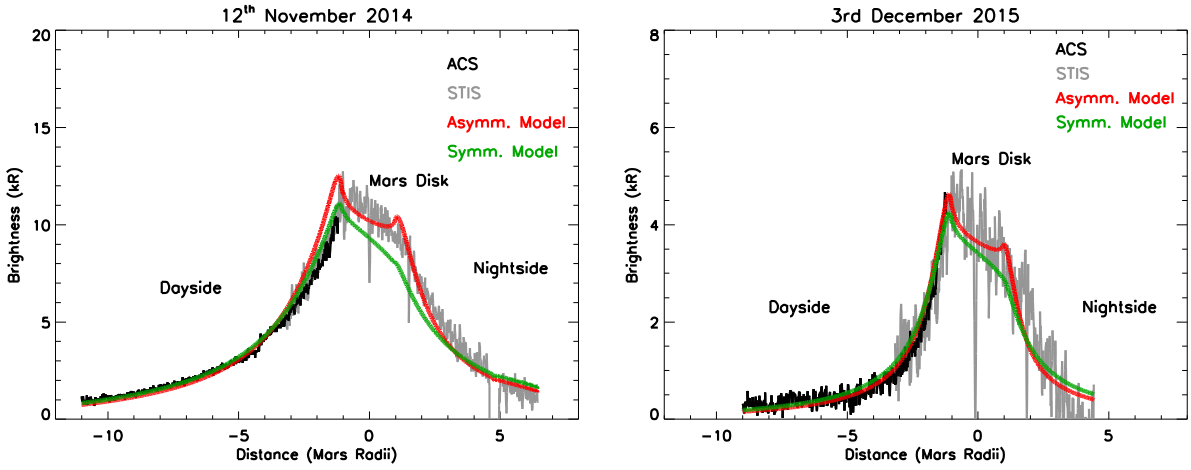


Figure 7: *Asymmetric and symmetric model fits to HST observations of the martian exospheric hydrogen Lyman α emission observed on 12th November 2014 and 3rd December 2015. The data consists of dayside exospheric observations with the ACS instrument along with the martian disk and night side observations with the STIS instrument onboard HST. The asymmetric model fits the disk and the night side intensities better than the symmetric model. The differences between the asymmetric and the symmetric model intensities become small above ~2.5 martian radii suggesting that the martian hydrogen exosphere approaches symmetry at higher altitudes.*

For modeling the HST observations using the 2-D RT model, first the 2-D density model was used to generate density profiles with thermal hydrogen exobase densities at SZA = 0° ranging from 1×10^4 cm^{-3} – 5×10^5 cm^{-3} (11 different density values). The exobase temperature at SZA = 0° for the two observation days were taken from the Mars Global Circulation Model (MGCM) [Chaufray et al., 2015; 2018]. MAVEN-NGIMS observations were not used here because MAVEN's orbit on these days did not sample close to the sub-solar point. The 2-D RT model was then used to simulate the emissivity of the atmosphere for each exobase density. The thermal H density that best matches the STIS observation up to ~2000 km through least-squares minimization was used to determine the thermal H population for that particular HST observation. The superthermal population of H atoms was determined through the same method as used in previous HST observation analysis [Bhattacharyya et al. 2015; 2017a; 2017b]. The temperature of the H superthermal population was taken to be 800 K. Different exobase densities for superthermal H ranging from 1×10^3 cm^{-3} – 4×10^4 cm^{-3} were added to the best-fit thermal density profile and the emissivity of the atmosphere was then determined using the 2-D RT model. The density of the superthermal population of H was not varied with SZA. The best-fit non-thermal density was then determined through chi-square minimization of the model fits to the ACS intensity profile, which extends from ~700 km to ~30,000 km and contains emissions from superthermal H atoms which become significant at higher altitudes (above ~20,000 km). Table 1 lists the best-fit thermal and superthermal H densities and temperatures for the two HST observation days. These values were then used in a symmetric 1-D model where the temperature and density varied only radially and not with SZA to simulate the intensity from a spherically symmetric and isothermal atmosphere. Figure 7 shows the comparison between the output from the symmetric and the asymmetric model for both the 12th November 2014 observation as well as the 3rd December 2015 observation of the martian hydrogen Lyman α emission HST. As is evident from the figure, the asymmetric model

689 fits the data better than the symmetric model, especially the disk brightness and the night side
690 brightness for the martian H corona. However, differences between the symmetric and the
691 asymmetric model intensities decrease above an altitude of ~2.5 martian radii as the martian
692 hydrogen exosphere approaches symmetry in conjunction with previous studies [Holmström,
693 2006; Bhattacharyya et al., 2017a; Chaufray et al., 2015]. The Jeans escape flux derived from the
694 symmetric model fits are greater than the asymmetric model fits to the data by a factor of 1.5 and
695 1.87 for the two HST observations.

696 **Table 1:** *Modeled characteristics of the hydrogen exosphere for the HST observations*

Date of Observation (day of year)	**Exobase temperature of thermal H at SZA = 0° T_{cold} (K)**	**Exobase density of thermal H at SZA = 0° N_{cold} (cm^{-3})**	**Exobase temperature of energetic H T_{hot} (K)**	**Exobase density of energetic H N_{hot} (cm^{-3})**	**Thermal H escape (atoms/sec)**	
					Asymmetric model	**Symmetric model**
12th November 2014 (316)	300	189000 ± 4000	800	10000 ± 2000	$6.23 \pm 0.14 \times 10^{26}$	$9.32 \pm 0.2 \times 10^{26}$
3rd December 2015 (337)	250	79000 ± 4000	800	5000 ± 4000	$8.54 \pm 0.44 \times 10^{25}$	$1.59 \pm 0.08 \times 10^{26}$

697

698 **5. Summary and Discussion**

699 Observations and analysis of the martian exospheric Lyman α emission in the past decade have
700 slowly revealed the complicated nature of this tenuous upper atmospheric layer. The presence of
701 a superthermal H component have been inferred from the analysis of Mars Express (MEX), HST
702 and MAVEN observations [Chaufray et al., 2008; Chaffin et al., 2014; 2015; Clarke et al., 2014;
703 Bhattacharyya et al., 2015]. These observations also revealed that the exosphere is not spherically
704 symmetric and isothermal [Holmström, 2006; Chaffin et al., 2015; Bhattacharyya et al., 2017a].

MAVEN-NGIMS observations of the lower thermosphere reported temperature differences of > 100 K between the day and the night side indicating a non-isothermal exosphere [Stone et al., 2018] and models imply a large difference in H density between subsolar and anti-solar point [Chaufray et al., 2018]. Therefore, in this study a more physically accurate 2-dimensional model of the martian exosphere based on MAVEN findings was constructed which would provide better constraints on the present-day escape rates of deuterium and hydrogen atoms from the exosphere of Mars. It is imperative to obtain an accurate value for the escape rate of H as it is tied to the escape of water from Mars, whereas an accurate estimate of the D/H ratio will help establish the timeline for the escape of the martian atmosphere throughout its history of evolution.

Uncertainties in estimating the D and H escape rate arise from both uncertainties in the data as well as the modeling process as was concluded from the Bhattacharyya et al. [2017] study. The data uncertainties are mostly dominated by the uncertainty in the instrumental absolute calibration [Bhattacharyya et al., 2017a]. A recent HST observation campaign utilized the STIS instrument onboard HST, whose absolute calibration is well-documented (within 5%) through observations of standard UV stellar sources, to determine the sensitivity of the ACS instrument at Lyman α. The ACS instrument, which is a broadband filter, has been used to image the H Lyman α emission from many different planetary hydrogen coronae, including Mars. Therefore, calibrating the ACS detector at Lyman α will help reduce the uncertainties associated with determining the H escape rate from Mars through analysis of HST ACS observations. The MAVEN-IUVS echelle Lyman α calibration factor was cross-checked with overlapping HST observations. However, the observed martian H Lyman α intensity by the MAVEN-IUVS echelle cannot be directly compared to the intensities recorded by HST due to the differences in their observing geometry. A 2-D radiative transfer model was utilized to obtain the characteristics of the martian hydrogen exosphere (hydrogen exobase density and temperature) for a particular day of observation (12th November 2014 and 3rd December 2015). This "best-fit" atmosphere for that particular day of observation was then used to simulate the H Lyman α intensities that would be observed by HST from the MAVEN-IUVS echelle observing geometry on that day. Assuming a 10% uncertainty in the modeling process, the MAVEN observed intensity, with its present calibration factor (including a 25% uncertainty), lies within the HST simulated intensity limits.

Model uncertainties are a result of the various assumptions made in the simulation process about the characteristics of the martian exosphere. Earlier models assumed a spherically symmetric

and isothermal exosphere. However, observations in the past decade have indicated an asymmetric non-isothermal exosphere below ~5000 km (~1.5 martian radii from the surface). Most of the spacecraft observations (MEX, and MAVEN) of the martian H and D Lyman α emissions are conducted at those altitudes. Therefore, in order to model the spacecraft observations a two-dimensional density model and a two-dimensional radiative transfer model was developed through this study. The density and temperature of the exospheric species were varied with altitude and solar zenith angle. This asymmetric model was then tested against results from the symmetric model by simulating MAVEN-IUVS Echelle observations of D and H Lyman α and HST observations of H Lyman α at Mars. In all cases the asymmetric model fit the data as well or better. The asymmetric model is particularly important for the comparison of observations at very different solar zenith angles, as is the case for the MAVEN mission.

For the HST observations, the asymmetric model better simulated the disk and the night side intensities than the symmetric model. The models converged above ~2.5 martian radii. Disparities between the 2-D model and the data below 2.5 martian radii could be due to local asymmetries in atmospheric characteristics that are not captured in the modeling process. Elevated densities for helium (by a factor of about 10 – 20) have been detected by MAVEN on the night side compared to the dayside [Elrod et al., 2017]. A larger concentration of helium was also detected in the polar regions compared to the equatorial regions. Similar asymmetries in H densities have been difficult to detect due to the optically thick nature of the Lyman α emission as well as the large expanse of the hydrogen exosphere. For D, the density is not large enough in the exosphere during most of the martian year (L_s = 330°- 220° through aphelion at L_s = 71°) to generate a Lyman α intensity which is detectable above the MAVEN-IUVS echelle detection threshold of ~100 Rayleighs. Therefore, MAVEN observations collected over the past 1.5 Mars years cannot detect large anomalies in densities. MAVEN orbit also precesses slowly around Mars in latitude and local solar time due to which only one perihelion (L_s = 251°) and southern summer solstice (L_s = 270°) coverage of the dayside deuterium emission was available in the dataset utilized in this study. This data is from late 2014 to early 2015 when MAVEN had just undergone its orbit insertion around Mars. The MAVEN-IUVS echelle observing geometries, integration times and detector binning schemes ideal for observing D and H Lyman α had not yet been established thereby resulting in degradation of the D Lyman α data. All these factors together could contribute towards the mismatch between the data and the 2-D model presented in this paper.

767 Jeans escape flux estimates for H from the HST simulations as listed in table 1 indicate that
768 a spherically symmetric model could overestimate the escape fluxes by more than a factor if 1.5.
769 Similar estimates have not been provided for D and H from the IUVS observations as the data is
770 heavily binned and contains a mixture of observations spanning from November 2014 – October
771 2017. In conclusion, the results of this study do establish that an asymmetric model is required to
772 simulate the D and H Lyman α emissions from the exosphere of Mars in order to better constrain
773 the total amount of water/atmospheric that has escaped Mars in its ~4.5 billion years of existence,
774 an important research goal currently being pursued by the Mars science community.

775

776 **Acknowledgements**

777 The first author thanks Jordan Montgomery and Sabyasachi Chatterjee for helpful discussions
778 about the mathematical derivations presented in the Vidal-Madjar and Bertaux [1972] paper. This
779 work was supported by NASA contract no. 1000320450 from the University of Colorado to Boston
780 University as well as Space Telescope Science Institute (STScI) grant GO-15098 to Boston
781 University. All HST data used in this study can be downloaded from the Space Telescope Science
782 Institute server at http://archive.stsci.edu/hst/search.php and all MAVEN data used in this study
783 are available on the NASA Planetary Data System at https://pds.nasa.gov/datasearch/subscription-
784 service/SS-20180215.shtml for release 12 of the IUVS level1a and level1c echelle dataset.

785

786 **Appendix A**

787 *A.1. Density distribution in a non-uniform and non-isothermal exosphere (above 200 km)*

788 The Chamberlain [1963] approach for deriving exospheric density distributions is a 1-dimensional
789 (1D) approach which assumes spherical symmetry. This approach was extended to 2-D/3-D by
790 Vidal-Madjar and Bertaux [1972] which is applicable to a non-spherically symmetric density
791 distribution in a planetary exosphere. Since collisions are negligible in the exosphere, the particles
792 still obey Liouville's theorem and follow the Maxwell-Boltzmann velocity distribution. For such
793 an asymmetric atmosphere, the distribution function at the critical altitude or the exobase is given
794 by:

$$f_c(\alpha_c, \delta_c, V_c) = N_c(\alpha_c, \delta_c)\left[\frac{1}{2\pi m k_b T_c(\alpha_c,\delta_c)}\right]^{3/2} exp\left[\frac{-mMGV_c^2}{r_c\, k_b\, T_c(\alpha_c,\delta_c)}\right] \quad \text{(A1.1)}$$

Here $N_c(\alpha_c, \delta_c)$ is the number density at the exobase as a function of the longitude, α_c and latitude, δ_c, m the mass of the species, k_b the Boltzmann's constant, $T_c(\alpha_c, \delta_c)$ the exobase temperature which is also a function of longitude and the latitude, r_c the exobase altitude (200 km for Mars), V_c the velocity at the exobase normalized to the escape velocity, M the mass of the planet and G the universal gravitational constant. Defining the following variables:

$$y = \frac{r_c}{r} \qquad\qquad V = \frac{v}{v_{esc}}$$

In the above expressions, r is an arbitrary radial distance from planet center and $v_{esc} = \sqrt{\frac{2GM}{r_c}}$.

The equations of motion of the particles in the collisionless exospheric regime which obey the law of conservation of energy and angular momentum can be written as:

$$V_c^2 - 1 = V^2 - y \quad \text{(A1.2)}$$

$$\frac{V \sin\theta}{y} = V_c \sin\theta_c \quad \text{(A1.3)}$$

The number density at any point in space can now be written as,

$$N(y, \alpha, \delta) = v_{esc}^3 \int N_c(\alpha_c, \delta_c)\left[\frac{m}{2\pi k_b T_c(\alpha_c,\delta_c)}\right]^{3/2} exp\left[\frac{-mMG\,(V^2+1-y)}{r_c\, k_b\, T_c(\alpha_c,\delta_c)}\right] V^2 \sin\theta\, dV d\theta d\varphi \quad \text{(A1.4)}$$

The above equation comes from Liouville's theorem which states that the density in phase space is conserved along dynamical trajectories. The integration is in momentum space over $V, \theta, and\ \varphi$ which are restricted to the existing trajectories that the particles might follow in the exosphere. There are three different types of trajectories that the particles can take which are,

- Ballistic trajectories where $V_c < 1$ or $V < \sqrt{y}$ with all the trajectories intersecting the exobase
- Escaping trajectories where $V_c > 1$ and $V > \sqrt{y}$
- Satellite trajectories which are created by small number of collisions which may take place between particles in the exosphere. The particles which follow the satellite trajectories are still bound by the planet's gravity and their trajectories do not cross the exobase level.

Since the number of collisions taking place in the exosphere is negligible, the total number of satellite particles present in the exosphere are considered to be negligible and has been ignored while modeling the martian exosphere.

A.1.1 Ballistic Particles

There is a velocity V_b at every radial distance r such that if $V < V_b$, the corresponding trajectory of the particle will intersect the exobase for any direction of the velocity vector. This velocity V_b corresponds to a trajectory whose apogee is r and perigee is r_c with $\sin\theta = \sin\theta_c = 1$. Applying this to equations (A1.2) and (A1.3) we have:

$$V_b = \frac{y}{\sqrt{1+y}} \tag{A1.5}$$

If $V > V_b$, then all trajectories do not reach the exobase. Only those trajectories which lie within a cone of half-angle θ_m whose axis is the local vertical, will have their perigees intersecting the exobase. With $\theta = \theta_m$ and $\sin\theta_c = 1$ in equations (A1.2) and (A1.3) we have:

$$\sin\theta_m = \frac{y}{V}\sqrt{V^2 + 1 - y} \tag{A1.6}$$

The ascending particles populate the region $0 < \theta < \theta_m$, whereas the descending particles populate the region $\pi - \theta_m < \theta < \pi$. The number density of ballistic particles at any radial distance will have the expression,

$$N_b(y,\alpha,\delta) = v_{esc}^3 \int_0^{V_b}\int_0^{\pi}\int_0^{2\pi} f_c\, V^2 \sin\theta\, dV\, d\theta\, d\varphi +$$

$$v_{esc}^3 \int_{V_b}^{\sqrt{y}}\int_0^{\theta_m}\int_0^{2\pi} f_c\, V^2 \sin\theta\, dV\, d\theta\, d\varphi + v_{esc}^3 \int_{V_b}^{\sqrt{y}}\int_{\pi-\theta_m}^{\pi}\int_0^{2\pi} f_c\, V^2 \sin\theta\, dV\, d\theta\, d\varphi \tag{A1.7}$$

The distribution function f_c has no θ or φ dependence and is only a function of the variables V_c, *and* α_c, δ_c through $N_c(\alpha_c, \delta_c)$ and $T_c(\alpha_c, \delta_c)$ dependence. Thus, in order to solve the above integral, first α_c *and* δ_c needs to be calculated and then the terms $N_c(\alpha_c, \delta_c)$ and $T_c(\alpha_c, \delta_c)$ need to be evaluated using the known functional dependence of the exobase density and temperature on the solar zenith angle. The density model presented here is only in 2-D. Therefore, in the modeling process the latitude $\delta = 0°$ which now renders the longitude angle α as the solar zenith angle. The variables α_c and δ_c is calculated using the following equations:

$$\delta_c(\alpha,\delta,\varphi,\psi) = sin^{-1}(\cos\delta\sin\psi\cos\varphi + \sin\delta\cos\psi) \tag{A1.8}$$

$$\psi = \beta - \beta_c \qquad \beta = cos^{-1}\left(\frac{y\omega(y,V,\theta) - r_c}{e(y,V,\theta)}\right) \qquad \beta_c = cos^{-1}\left(\frac{\omega(y,V,\theta) - r_c}{e(y,V,\theta)}\right)$$

$$\omega = 2r_c\frac{V^2\, sin^2\theta}{y^2} \qquad e = \sqrt{1 - \frac{4V^2\, sin^2\theta\,(y - V^2)}{y^2}}$$

$$\alpha_c(\alpha,\delta,\varphi,\psi) = cos^{-1}\left(\frac{-\sin\delta\cos\alpha\sin\psi\cos\varphi + \sin\alpha\sin\psi\sin\varphi + \cos\delta\cos\alpha\cos\psi}{\cos\delta_c(\alpha,\delta,\varphi,\psi)}\right) \tag{A1.9}$$

The solar zenith angle can be written as $\gamma = cos^{-1}(\cos\alpha_c \cos\delta_c)$ and because of the symmetry in the 3rd dimension, $N_c(\alpha_c, \delta_c) = N_c(\gamma)$ and $T_c(\alpha_c, \delta_c) = T_c(\gamma)$.

A.1.2 Escaping Particles

Under this condition, all trajectories which result in escape from the parent body's gravitational potential are considered. These trajectories also lie within a cone of half-angle θ_m ($0 < \theta < \theta_m$), the expression for which is given by the relation depicted in equation (A1.6). The number density of escaping particles at any radial distance from the planet's center is given by the expression:

$$N_e(y, \alpha, \delta) = v_{esc}^3 \int_{\sqrt{y}}^{\infty} \int_0^{\theta_m} \int_0^{2\pi} f_c \, V^2 \sin\theta \, dV \, d\theta \, d\varphi \qquad \text{(A2.0)}$$

The distribution function f_c has no θ or φ dependence and is only a function of the variable V_c, *and* α_c, δ_c through $N_c(\alpha_c, \delta_c)$ and $T_c(\alpha_c, \delta_c)$ dependence, same as the ballistic particle case.

A.2. Density distribution below 200 km

The density distribution below the exobase is estimated using a simple diffusion model in which only the diffusion of H or D in CO_2 is considered [Bhattacharyya et al., 2017a]. The diffusion equation from Hunten [1973] is of the form:

$$\Phi_H(r) = -(D_H + K)\frac{dn_H}{dr} - \left[D_H\left(\frac{GMm_H}{kT(r)r^2} + \frac{1+\alpha_T}{T}\frac{dT}{dr}\right) + K\left(\frac{GM\mu}{kT(r)r^2} + \frac{1}{T}\frac{dT}{dr}\right)\right] n_H \qquad \text{(A2.1)}$$

In the above equation, D_H is the diffusion coefficient of H or D in CO_2 given by $D_H(r) = \frac{AT(r)^s}{n_{CO_2}(r)}$, A = 8.4 x$10^{17}$ cm^2 s^{-1} for H and A = 1.0 x10^{17} cm^2 s^{-1} for D; s = 0.6 for H and s = 0.75 for D [Hunten, 1973]. K is the eddy diffusion co-efficient and has the expression $K(h) = 1.2 \times 10^{12}\sqrt{\frac{T_\infty}{n(h)}}\ cm^2 s^{-1}$ [Krasnopolsky, 2002]. The thermal coefficient factor α_T equals -0.25 for both H and D (Krasnopolsky, 2002). Upon solving the diffusion equation for each SZA, the number density with altitude and SZA can be derived for either D or H at Mars [Chaufray et al., 2008; Bhattacharyya et al., 2017a].

Appendix B

B.1. Radiative transfer model for a non-symmetric, non-isothermal atmosphere

A photon when it passes through a medium, its characteristics such as wavelength, frequency and direction of propagation, may be altered because of interaction with the medium. The process of radiative transfer and the relevant equations describe the physical process governing the interaction of the photon with the surrounding medium. The solution of these equations applied to a specific problem provides the means of accurately simulating the radiation field in various environments. In this section, the radiative transfer process in a non-spherically symmetric and non-isothermal environment is explored and the relevant equations that describe this process are derived.

The general equation of radiative transfer in a medium is given by the relation:

$$\frac{dI_\upsilon(\boldsymbol{r},\theta,\varphi)}{ds} = -\kappa_\upsilon^{ext}(\boldsymbol{r})\, I_\upsilon(\boldsymbol{r},\theta,\varphi) + S_\upsilon(\boldsymbol{r},\theta,\varphi) \quad \text{(B1.1)}$$

In the above equation, $I_\upsilon(\boldsymbol{r},\theta,\varphi)$ is the intensity (photons cm^{-2} s^{-1} Hz^{-1} sr^{-1}), $S_\upsilon(\boldsymbol{r},\theta,\varphi)$ the volume emission rate or source function (photons cm^{-3} s^{-1} sr^{-1} Hz^{-1}) and $\kappa_\upsilon^{ext}(\boldsymbol{r})$ the extinction coefficient (cm^{-1}) which is a sum of the scattering and absorption coefficients. The formal solution to equation (B1.1) as presented by Chandrasekhar [1960] can be written as:

$$I_\upsilon(\boldsymbol{r},\theta,\varphi) = I_\upsilon(\boldsymbol{r}_\infty,\theta,\varphi)e^{-\tau_\upsilon(r,r_\infty)} + \int_{\boldsymbol{r}}^{r_\infty} S_\upsilon(\boldsymbol{r}',\theta,\varphi)\, e^{-\tau_\upsilon(r,r')}\, ds' \quad \text{(B1.2)}$$

In the above equation which describes the intensity along a line of sight through a medium, the term $I_\upsilon(\boldsymbol{r}_\infty,\theta,\varphi)$ describes the contribution to the line of sight intensity from sources external to the medium, the term $e^{-\tau_\upsilon(r,r_\infty)}$ describes the attenuation of the line of sight intensity (scattering and absorption within the medium as well as external to the medium), the term $S_\upsilon(\boldsymbol{r}',\theta,\varphi)$ is the source function due to scattering of photons within the medium and $e^{-\tau_\upsilon(r,r')}$ the attenuation (scattering and absorption) within the medium. In the absence of external sources, the above equation reduces to:

$$I_\upsilon(\boldsymbol{r},\theta,\varphi) = \int_r^{r_\infty} S_\upsilon(\boldsymbol{r}',\theta,\varphi)\, e^{-\tau_\upsilon(r,r')}\, ds' \quad \text{(B1.3)}$$

The source function term is a combination of scattering from internal and external sources.

$$S_\upsilon(\boldsymbol{r},\theta,\varphi) = S_\upsilon^{ext}(\boldsymbol{r},\theta,\varphi) + S_\upsilon^{int}(\boldsymbol{r},\theta,\varphi)$$

Internal sources of radiation like photoelectron impact excitation, etc. are ignored in the modeling process presented in this paper. The external source function has the form:

$$S_\upsilon^{ext}(\boldsymbol{r},\theta,\varphi) = \frac{b}{4\pi}\int_0^\infty d\upsilon'\, \kappa_{\upsilon'}^{sca}(\boldsymbol{r}) \int d\Omega'\, R(\boldsymbol{r};\upsilon,\upsilon',\Omega,\Omega')\, I_\upsilon(\boldsymbol{r}_\infty,\theta',\varphi')e^{-\tau_{\upsilon'}(r,r_\infty)} \quad \text{(B1.4)}$$

In the above equation, b is the branching ratio for the transitions from the excited upper state to the ground state, $\kappa_{\upsilon'}^{sca}(\boldsymbol{r})$ the scattering coefficient, $d\Omega'$ the angular element in which the resonant scattering occurs, $R(\boldsymbol{r};\upsilon,\upsilon',\Omega,\Omega')$ the scattering redistribution function, $I_\upsilon(\boldsymbol{r}_\infty,\theta',\varphi')$ the

intensity of the incident radiation at the top of the atmosphere, and $e^{-\tau_{\upsilon'}(\boldsymbol{r},\boldsymbol{r}_\infty)}$ the attenuation due to absorption and scattering of the incident radiation along a line of sight.

If the medium is optically thick, then the external source term is a combination of the single and multiple scattering source function. In the case of Mars, the hydrogen exosphere resonantly scatters solar Lyman α photons. Therefore, the single scattering term will merely describe the scattering of the solar Lyman α photons by the martian hydrogen exosphere. The single scattering source function for the process of resonant scattering of solar photons by martian H atoms can be written as:

$$S_{\upsilon}^{Sun}(\boldsymbol{r},\theta,\varphi) = b\int_0^{\infty} d\upsilon'\,\kappa_{\upsilon'}^{sca}(\boldsymbol{r})\int d\Omega'\; R(\boldsymbol{r};\upsilon,\upsilon',\Omega,\Omega_{Sun})\;\pi F_{Sun}(\upsilon')\,e^{-\tau_{\upsilon'}(\boldsymbol{r},\boldsymbol{r}_{Sun})} \quad \text{(B1.5)}$$

Isotropic scattering of the solar photons is considered which reduces $\int d\Omega' = \int_0^{\pi} sin\,\theta' d\theta' \int_0^{2\pi} d\varphi' = 4\pi$ and removes the Ω dependency from the redistribution function. Therefore, $R(\boldsymbol{r};\upsilon,\upsilon',\Omega,\Omega_{Sun}) = R(\boldsymbol{r};\upsilon,\upsilon')$.

The atmosphere considered in the model is symmetric in the φ direction in the spherical polar coordinate system, but is variable in the $\boldsymbol{r}$ and θ direction. Here forth, the variable $\boldsymbol{r}$ in the equations will represent dependency in both the *r* (radial) and θ (SZA) direction. The sun is taken to be along the z axis in the model. Therefore, θ represents the solar zenith angle in the model.

For solving equation (B1.5) for a non-symmetrical, non-isothermal atmosphere, we define the following variables:

$$x(\boldsymbol{r}) = \frac{\upsilon-\upsilon_0}{\Delta\upsilon_D(\boldsymbol{r})} \quad (B1.6a); \quad d\upsilon = dx\,\Delta\upsilon_D(\boldsymbol{r}) \quad (B1.6b); \quad \Delta\upsilon_D(\boldsymbol{r}) = \frac{\upsilon_0}{c}\sqrt{\frac{2k_bT(\boldsymbol{r})}{m}} \quad (B1.6c)$$

Define a constant reference temperature T_{ref}, which corresponds to the highest temperature value for the entire atmosphere for a particular day. Therefore, the terms in equations (B1.6a), (B1.6b) and (B1.6c) will have their reference counterparts, which has no dependence on r, since T_{ref} is a constant. Now, writing the variables $x(\boldsymbol{r})$, and $\Delta\upsilon_D(\boldsymbol{r})$ in terms of the reference temperature, we have:

$$x(\boldsymbol{r}) = x_{ref}\sqrt{\frac{T_{ref}}{T(\boldsymbol{r})}} \quad (B1.7a); \qquad \Delta\upsilon_D(\boldsymbol{r}) = \Delta\upsilon_{D_{ref}}\sqrt{\frac{T(\boldsymbol{r})}{T_{ref}}} \quad (B1.7b)$$

Also, the scattering cross section can now be written as:

$$\sigma_0(\boldsymbol{r}) = \sigma_{ref}\sqrt{\frac{T_{ref}}{T(\boldsymbol{r})}} \quad (B1.8) \qquad \text{where, } \sigma_{ref} = \frac{5.96\times10^{-12}}{\sqrt{T_{ref}}}$$

Now, expanding upon each of the terms in equation (B1.5):

$b = 1$ for resonant scattering of Lyman α photons by H atoms.

$dv' = dx'\,\Delta v_D(\boldsymbol{r})$ which is derived from equation (B1.6b).

$\kappa_{v'}^{sca}(\boldsymbol{r}) = n(\boldsymbol{r})\,\sigma_0(\boldsymbol{r})\,e^{-x'^2(\boldsymbol{r})}$, where $\kappa_{v'}^{sca}(\boldsymbol{r})$ represents the resonant scattering cross section and $n(\boldsymbol{r})$ the number density at any point $\boldsymbol{r}$ in the atmosphere.

$R(\boldsymbol{r}; v, v') = R(x, x') = \frac{1}{\pi}\,e^{-x'^2}\,e^{-x^2}$; This function is related to Hummer's [Hummer, 1962] by

$R(x, x') = \frac{\frac{1}{\pi}\,e^{-x'^2}\,e^{-x^2}}{\frac{1}{\pi\,\Delta v_D(r)}\int_{-\infty}^{\infty} dx\,e^{-x'^2}\,e^{-x^2}}$ and $\int_{-\infty}^{\infty} e^{-x^2} = \sqrt{\pi}$.

$R(x, x') = \frac{e^{-x^2(r)}}{\sqrt{\pi}\,\Delta v_D(\boldsymbol{r})}$, is the final form of the redistribution function. This form of the function considers the process of complete frequency redistribution which is true for moderately thick resonance lines and is applicable to the martian Lyman α emission.

$\pi F_{Sun}(v') = F_0 = constant$, represents the solar Lyman α flux at line center for a particular day. In general, this flux should vary with frequency, but for Mars the Lyman α emission line is extremely narrow due to the cold atmospheric temperatures and the majority of the H atoms only scatter near the line center where the variation of flux with frequency is negligible.

$e^{-\tau_{v'}(\boldsymbol{r}, \boldsymbol{r_{Sun}})}$ represents the sum of scattering by H atoms as well as the absorption by CO_2 of the Lyman α photons in the martian atmosphere along any line of sight. The absorption and the scattering terms can be written as:

absorption by CO_2: $e^{-\tau_{CO_2}(\boldsymbol{r},\,\boldsymbol{r_{Sun}})} = exp\left\{-\int_{\boldsymbol{r}}^{\boldsymbol{r_{Sun}}} n_{CO_2}(\boldsymbol{r'})\;\sigma_{CO_2}(\boldsymbol{r'})\,ds'\right\}$. The cross section of absorption of Lyman α photons by CO_2 is dependent upon temperature and does not have any analytical formula. However, laboratory measurements exist for the same [Venot et al., 2018].

Scattering by H: $exp\left\{-\int_{\boldsymbol{r}}^{\boldsymbol{r_{Sun}}} n(\boldsymbol{r'})\,\sigma_0(\boldsymbol{r'})\,e^{-x'^2(\boldsymbol{r'})}\,ds'\right\}$

Substituting these expressions in equation (B1.5) we have:

$$\frac{S_x^{Sun}(\boldsymbol{r})}{\Delta v_D(\boldsymbol{r})} = \frac{F_0\,\Delta v_D(\boldsymbol{r})\,n(\boldsymbol{r})\,\sigma_0(\boldsymbol{r})}{\sqrt{\pi}\,\Delta v_D(\boldsymbol{r})}\,e^{-\tau_{CO_2}(\boldsymbol{r},\,\boldsymbol{r_{Sun}})}e^{-x^2(\boldsymbol{r})}$$

$$\times \int_{-\infty}^{\infty} dx' e^{-x'^2(\boldsymbol{r})} exp\left\{-\int_{\boldsymbol{r}}^{\boldsymbol{r_{Sun}}} n(\boldsymbol{r'})\,\sigma_0(\boldsymbol{r'})\,e^{-x'^2(\boldsymbol{r'})} ds'\right\} \qquad \text{(B1.8)}$$

Upon integrating over x on both sides,

$$\int_{-\infty}^{\infty} S_x^{Sun}(\boldsymbol{r}) = S_0^{Sun}(\boldsymbol{r});\quad and\quad \int_{-\infty}^{\infty} dx\,e^{-x^2(\boldsymbol{r})} = \sqrt{\pi}$$

Therefore, equation (B1.8) reduces to

$$S_0^{Sun}(\boldsymbol{r}) =$$

$$g\, n(\boldsymbol{r})\, e^{-\tau_{CO_2}(r,\, r_{Sun})}\, \frac{1}{\sqrt{\pi}} \int_{-\infty}^{\infty} dx' e^{-x'^2(r)} exp\left\{ - \int_{\boldsymbol{r}}^{r_{Sun}} n(\boldsymbol{r'})\, \sigma_0(\boldsymbol{r'})\, e^{-x'^2(r')} ds' \right\} \quad \text{(B1.9)}$$

In the above equation g is the excitation frequency given by equation $g = \sqrt{\pi}\, \Delta\upsilon_{D_{ref}} \sigma_{ref}\, F_0$. Every x term and σ term in equation (B1.9) can be written in terms of their reference temperature counterpart using equations (B1.7a, B1.7b and B1.8) which leaves the source function to be dependent on temperature and density, both of which vary with r and θ.

For the multiple scattering source function, which is derived from equation (B1.4) has the form:

$$S_{\upsilon}^{mult}(\boldsymbol{r}) = \frac{b}{4\pi} \int_0^{\infty} d\upsilon'\, \kappa_{\upsilon'}^{sca}(\boldsymbol{r}) \left\{ \int d\Omega'\, R(\boldsymbol{r}; \upsilon, \upsilon') \int_r^{r_\infty} S_{\upsilon'}(\boldsymbol{r'})\, e^{-\tau_{\upsilon'}(r,r')}\, ds' \right\} \quad \text{(B2.0)}$$

In the above equation the term $S_{\upsilon'}(\boldsymbol{r'})$, which has a dependence on frequency υ, can be written as:

$$S_{\upsilon'}(\boldsymbol{r'}) = S(\boldsymbol{r'})\, \frac{e^{-x'^2(\boldsymbol{r})}}{\sqrt{\pi}\, \Delta\upsilon_D(\boldsymbol{r})}$$

The forms of the various terms are already known from calculating the single scattering source function. However, unlike for the single scattering source function, the $\int d\Omega'$ term does not reduce to 4π. Substituting the various terms in equation (B2.0) we have:

$$\frac{S_x^{Mult}(\boldsymbol{r})}{\Delta\upsilon_D(\boldsymbol{r})} = n(\boldsymbol{r})\, \sigma_0(\boldsymbol{r}) \left(\int \frac{d\Omega'}{4\pi} \right) \frac{e^{-x^2(\boldsymbol{r})}}{\sqrt{\pi}} \int_{-\infty}^{\infty} dx'\, e^{-x'^2(\boldsymbol{r})}$$

$$\times \left(\int_{\boldsymbol{r}}^{r_\infty} ds'\, S(\boldsymbol{r'}) \frac{e^{-x'^2(\boldsymbol{r'})}}{\sqrt{\pi}\, \Delta\upsilon_D(\boldsymbol{r'})}\, e^{-\tau_{CO_2}(\boldsymbol{r},\boldsymbol{r'})} exp\left\{ - \int_{r_i}^{r_j} n(\boldsymbol{r''})\, \sigma_0(\boldsymbol{r''})\, e^{-x''^2} ds \right\} \right) \quad \text{(B2.1)}$$

Taking the integral of x on both sides, the above equation reduces to the following:

$$S_0^{mult}(\boldsymbol{r}) = n(\boldsymbol{r})\, \sigma_{ref} \left(\int \frac{d\Omega'}{4\pi} \right) \int_r^{r_\infty} ds'\, S(\boldsymbol{r'})\, e^{-\tau_{CO_2}(\boldsymbol{r},\boldsymbol{r'})} \sqrt{\frac{T_{ref}}{T(\boldsymbol{r'})}}$$

$$\times \frac{1}{\sqrt{\pi}} \int_{-\infty}^{\infty} dx'\, e^{-x'^2(\boldsymbol{r})}\, e^{-x'^2(\boldsymbol{r'})}\, exp\left\{ - \int_{r_i}^{r_j} n(\boldsymbol{r''})\, \sigma_0(\boldsymbol{r''})\, e^{-x''^2} ds \right\} \quad \text{(B2.2)}$$

With the expressions for the single and multiple scattering source functions, the total source function at any point $\boldsymbol{r}$ in the atmosphere can be written as:

$$S_{tot}(\boldsymbol{r}) = S_0^{Sun}(\boldsymbol{r}) + S_0^{mult}(\boldsymbol{r}) \quad \text{(B2.3)}$$

The multiple scattering source function has the term $S(\boldsymbol{r'})$ in it which prevents the derivation of an analytical expression for the total source function. In order to solve the above equation, an

iterative approach is undertaken, where the first term is taken to be the zero-order solution [Bertaux, 1974; Quémerais and Bertaux, 1993]. Under this approach, equation (B2.3) is discretized and represented by the vectorial relation:

$$\vec{S}_{n+1} = \vec{S}_0 + [A].\vec{S}_n \tag{B2.4}$$

In the above equation $\vec{S}_{n+1}$ is the vector containing the source function values at all the grid points in the atmosphere after $n+1$ iterations, $\vec{S}_0$ is the vector containing the single scattering source function at all the grid points, $[A]$ is the matrix of influence which contains information on the influence of all the grid points on every grid point due to the process of multiple scattering and $\vec{S}_n$ represents the total scattering source function (single and multiple) at all the grid points after the nth iteration. The matrix of influence is given by the expression:

$$a_{ij} = \sum_{\Omega_{ij}} \sigma_{ref}\, n_i \frac{\mathrm{d}\Omega_{ij}}{4\pi} e^{-\tau_{CO_2 ij}} \sqrt{\frac{T_{ref}}{T(\boldsymbol{r}_{ij})}} \frac{1}{\sqrt{\pi}} \int_{-\infty}^{\infty} dx_i\, e^{-x_i^2} e^{-x_j^2} exp\left\{ -\int_{r_i}^{r_k} n_{ik}\, \sigma_{0_{ik}} e^{-x_{ik}^2}\, ds_k \right\} ds_j \tag{B2.5}$$

The dimensionless coefficient a_{ij} represents the contribution to the source function at grid point *j* due to multiple scattering at grid point *i.* $\mathrm{d}\Omega_{ij}$ is the solid angle within which point *i* sees point *j*. The iteration represented in equation (B2.4) is conducted until convergence is achieved which is determined by the condition:

$$\frac{\overrightarrow{||\vec{S}_{n+1} - \vec{S}_n||}}{||\vec{S}_{n+1}||} \leq \delta = 1 \times 10^{-5} \tag{B2.6}$$

The norm of the vector indicates the maximum value for the vector.

References

Ajello, J., A. I. Stewart, G. Thomas, A. Graps (1987), Solar cycle study of interplanetary Lyman-alpha variations – Pioneer Venus orbiter sky background results, *J. Astrophys., 317,* p. 964 – 986.

Anderson, D. E., and C.W. Hord (1971), Mariner 6 and 7 Ultraviolet Spectrometer Experiment: Analysis of Hydrogen Lyman-Alpha Data, *J. Geophys. Res., 76*, 6666-6673

Anderson, D. E., Hord C. W. (1972), Correction. *J. Geophys. Res., 77,5638*

1007 Anderson, D. E. (1974), Mariner 6, 7 and 9 Ultraviolet Spectrometer Experiment: Analysis of
1008 Hydrogen Lyman Alpha Data, *J. Geophys. Res., 79,* 1513-1518

1009 Babichenko, S.I., Deregusov, E. V., Kurt, V. G., Romanova, N. N., Skljankin, V. A., Smirnov, A.
1010 S., J.- L. Bertaux, J. Blamont (1977), Measurements in Interplanetary Space and in the martian
1011 Upper Atmosphere with a Hydrogen Absorption-cell Spectrophotometer for L-alpha Radiation
1012 On-board Mars 4-7 Space probes, *Space Science Instrumentation, vol. 3*, p. 271-286

1013 Barth, C., W. Fastie, C. Hord, J. Pearce, K. Kelly, A. Stewart, G. Thomas, G. Anderson, O. Raper
1014 (1969), Mariner 6 Ultraviolet Spectrum of Mars Upper Atmosphere. *Science 165,* 1004-1005

1015 Bertaux, J. L. (1974), L'hydrogène atomique dans l'exosphère terrestre : mesures d'intensité et
1016 de largeur de raie de l'émission Lyman-alpha à bord du satellite OGO-5 et interprétation, Ph.D.
1017 Thesis, University of Paris 6 Pierre et Marie Curie.

1018 Bertaux, J. L., Clarke, J. T., Mumma, M. J., Owen, T., Quemerais, E. (1993), A Search for the
1019 Deuterium Lyman-alpha Emission from the Atmosphere of Mars, in "*Science with the Hubble*
1020 *Space Telescope"*, ESO Proc. No. 44, 459-462

1021 Bhattacharyya, D., J. T. Clarke, J. L. Bertaux, J. Y. Chaufray, M. Mayyasi (2015), A Strong
1022 Seasonal Dependence in the Martian Hydrogen Exosphere, *Geophys. Res. Lett., 42,* p. 8678-8685.

1023 Bhattacharyya, D., J. T. Clarke, J. L. Bertaux, J. Y. Chaufray, M. Mayyasi (2017a), Analysis and
1024 Modeling of Remote Observations of the Martian Hydrogen Exosphere, *Icarus, 281,* p. 264-280.

1025 Bhattacharyya, D., J. T. Clarke, J. Y. Chaufray, M. Mayyasi, J. L. Bertaux, M. S. Chaffin, N. M.
1026 Schneider, G. L. Villanueva (2017b), Seasonal Changes in Hydrogen Escape from Mars Through
1027 Analysis of HST Observations of the Martian Exosphere Near Perihelion, *J. Geophys. Res., 122,*
1028 p. 11756-11764.

1029 Bougher, S., D. Pawlowski, J. Bell, S. Nelli, T. McDunn, J. Murphy, M. Chizek, and A. Ridley (
1030 2015), Mars Global Ionosphere-Thermosphere Model: Solar cycle, seasonal, and diurnal
1031 variations of the Mars upper atmosphere, *J. Geophys. Res.: Planets, 120,* p. 311-342.

1032 Chaffin, M. S., Chaufray, J. Y., Stewart, I., Montmessin, F., Schneider, N. M., Bertaux, J. L.
1033 (2014), Unexpected Variability of Martian Hydrogen Escape, *Geophys. Res. Lett., 41,* 314-320.

1034 Chaffin, M. S., et al. (2015), Three-dimensional structure in the Mars H corona revealed by IUVS
1035 on MAVEN, *Geophys. Res. Lett., 42,* p. 9001-9008.

1036 Chaffin, M. S., J. Deighan, N. Schneider, A. I. F. Stewart (2017), Elevated atmospheric escape of
1037 atomic hydrogen from Mars induced by high-altitude water, *Nature Geoscience, 10,* p. 174-178.

1038 Chaffin, M., et al. (2018), Mars H escape rates derived from MAVEN/IUVS Lyman alpha
1039 brightness measurements and their dependence on model assumptions, *J. Geophys. Res., 123*, p.
1040 2192–2210, https://doi.org/10.1029/2018JE005574

1041 Chamberlain, J. W. (1963), Planetary Coronae and Atmospheric Evaporation, *Planetary & Space*
1042 *Science, 8,* p. 901-960.

1043 Chaufray, J. Y., Bertaux, J. L., LeBlanc, F., Quemerais, E. (2008), Observation of the Hydrogen
1044 Corona with SPICAM on Mars Express, *Icarus, 195,* 598-613

1045 Chaufray, J. Y., Gonzalez-Galindo, F., Forget, F., Lopez-Valverde, M. A., LeBlanc, F., Modolo,
1046 R., Hess, S. (2015), Variability of the Hydrogen in the Martian Upper Atmosphere as Simulated
1047 by a 3D Atmosphere-Exosphere Coupling, *Icarus, 245,* 282-294.

1048 Chaufray, J.-Y., R. V. Yelle, F. Gonzalez-Galindo, F. Forget, M. Lopez-Valverde, F. Leblanc, R.
1049 Modolo (2018), Effect of the lateral exospheric transport on the horizontal hydrogen distribution
1050 near the exobase of Mars, *J. Geophys. Res.: Space Physics, 123,* p. 2441-2454.

1051 Clarke, J. T., J. Bertaux, J. Y. Chaufray, G. Gladstone, E. Quemerais, J. Wilson, D. Bhattacharyya
1052 (2014), A Rapid Decrease of the Hydrogen Corona of Mars, *Geophys. Res. Lett., 41,* 8013-8020.

1053 Clarke, J. T., *et al.* (2017), Variability of D and H in the martian upper atmosphere observed with
1054 the MAVEN IUVS echelle channel. *J. Geophys. Res.: Space Physics*, *122*, 2336–2344, doi:
1055 10.1002/2016JA023479

1056 Clarke, J. (2018), Dust-enhanced water escape, *Nature*, https://doi.org/10.1038/s41550-018-0383-
1057 6

1058 Dostovalev, S. B., and Chuvakhin, S. D. (1973), On the Distribution of Neutral Hydrogen in the
1059 Upper Atmosphere of Mars, *Cosmic Research, 11,* 767-773.

1060 Elrod, M. K., S. Bougher, J. Bell, P. R. Mahaffy, M. Benna, S. Stone, R. V. Yelle, B. Jakosky
1061 (2017), He bulge revealed: He and CO_2 diurnal and seasonal variation in the upper atmosphere of

1062 Mars as detected by MAVEN NGIMS, *J. Geophys. Res.: Space Physics, 122,*
1063 doi:10.1002/2016JA023482.

1064 Emerich, C., Lemaire, P., Vial, J. C., Curdt, W., Schule, U., Wilhelm, K. (2005), A New Relation
1065 Between the Central Spectral Solar H I Lyman α Irradiance and the Line Irradiance Measured by
1066 SUMER/SOHO During the Cycle 23, *Icarus, 178,* 429-433.

1067 Eparvier, F., P. Chamberlin, T. Woods, E. Thiemann, (2015), The solar extreme ultraviolet monitor
1068 for MAVEN, Space Science Reviews, 195(1-4), 293–301, doi:10.1007/s11214-015-0195-2

1069 Fedorova, A., J. L. Bertaux, D. Betsis, F. Montmessin, O. Korablev, L. Maltagliati, J. Clarke
1070 (2017), Water vapor in the middle atmosphere of Mars during the 2007 global dust storm, *Icarus,*
1071 *300,* p. 440-457.

1072 Forget, F., Hourdin, F., Fournier, R., Hourdin, C., Talagrand, O., Collins, M., Lewis, S. R., et al.
1073 (1999). Improved general circulation modelsof the Martian atmosphere from the surface to above
1074 80 km, *Journal of Geophysical Research*,104(E10), 24,155–24,175.
1075

1076 Halekas, J. S. (2017), Seasonal variability of the hydrogen exosphere of Mars, *J. Geophys. Res.*
1077 *Planets*, *122*, doi:10.1002/2017JE005306.

1078 Heavens, N., A. Kleinböhl, M. Chaffin, J. Halekas, D. Kass, P. Hayne, D. McCleese, S. Piqeux, J.
1079 Shirley, and J. Schofield (2018), Hydrogen escape from Mars enhanced by deep convection in dust
1080 storms, *Nature*, 2, 126 – 132, doi: 10.1038/s41550-017-0353-4.

1081 Hodges, R. R. Jr., and F. S. Johnson (1968), Lateral transport in planetary atmospheres, *J. Geophys.*
1082 *Res., 73,* p. 7307.

1083 Holmström, M (2006), Asymmetries in Mars' Exosphere. Implications for X-ray and ENA
1084 Imaging, *Space Science Reviews, 126,* p. 435-445.

1085 Hummer, D. G. (1962), Non-coherent scattering, I, The redistribution functions with Doppler
1086 broadening, *Mon. Not. R. Astron. Soc., 125,* p. 21-37.

1087 Hunten, D. M., and McElroy, M. B. (1970), Production and Escape of Hydrogen on Mars, *J.*
1088 *Geophys. Res., 75,* 5989-6001

1089 Hunten, D. M. (1973), The Escape of Light Gases from Planetary Atmospheres, *J. Atmos. Sci., 30,*
1090 1481-1494

1091 Hunten, D. M. (1982), Thermal and Non-Thermal Escape Mechanisms for Terrestrial Bodies,
1092 *Planetary & Space Sciences, 30,* p. 773-783.

1093 Krasnopolsky, V. A., Mumma, M. J., Gladstone, G. R. (1998), Detection of Atomic Deuterium in
1094 the Atmosphere of Mars, *Science, 280,* p. 1576-1580

1095 Krasnopolsky, V. A. (2002), Mars' Upper Atmosphere and Ionosphere at Low, Medium and High
1096 Solar Activities: Implications for Evolution of Water, *J. Geophys. Res., 107,* 11-1-11-1

1097 Lewis, S. R., Collins, M., Read, P. L., Forget, F., Hourdin, F., Fournier, R., Hourdin, C., et al.
1098 (1999). A climate database for Mars.Journal ofGeophysical Research,104(E10), 24,177–24,194.
1099
1100 Mahaffy, P. R., *et al.* (2015a), The Neutral Gas and Ion Mass Spectrometer on the Mars
1101 Atmosphere and Volatile Evolution Mission, *Sp. Sci. Rev., 195,* p. 49-73.

1102 Mahaffy, P. R., et al. (2015b), The Imprint of Atmospheric Evolution in the D/H of Hesperian
1103 Clay Minerals on Mars, *Science, 347,* p. 412-414.

1104 Mahaffy, P. R., M. Benna, M. Elrod, R. V. Yelle, S. W. Bougher, S. W. Stone, and B. M. Jakosky
1105 (2015c), Structure and composition of the neutral upper atmosphere of Mars from the MAVEN
1106 NGIMS investigation, *Geophys. Res. Lett., 42,* doi:10.1002/2015GL065329.

1107 Matta, M., P. Withers and M. Mendillo (2013), The composition of Mars' topside ionosphere:
1108 Effects of hydrogen, *J. Geophys. Res.: Space Physics, 118,* p. 2681-2693.

1109 Mayyasi, M., et al. (2017a). IUVS echelle-mode observations of interplanetary hydrogen: Standard
1110 for calibration and reference for cavity variations between Earth and Mars during MAVEN cruise.
1111 *J. Geophys. Res.: Space Physics, 122*, doi:10.1002/2016JA023466

1112 Mayyasi, M., et al. (2017b). The variability of atmospheric deuterium brightness at Mars: Evidence
1113 for seasonal dependence. *J. Geophys. Res.: Space Physics, 122*, doi:10.1002/2017JA024666

1114 Mayyasi, M., Bhattacharyya, D., Clarke, J., Catalano, A., Benna, M., Mahaffy, P., et al. (2018),
1115 Significant Space Weather Impact on the Escape of Hydrogen from Mars, *Geophys. Res. Let.*, *45*,
1116 p. 8844-8852, https://doi.org/10.1029/2018GL077727.

1117 Mayyasi, M., et al. (2019), Seasonal variability of deuterium in the upper atmosphere of Mars, *J.*
1118 *Geophys. Res.,* doi:10.1029/2018JA026244.

McClintock, W. E., *et al.* (2015), The Imaging Ultraviolet Spectrograph (IUVS) for the MAVEN mission, *Sp. Sci. Rev., 195,* p. 75-124.

McElroy, M. B., and Donahue T. M. (1972), Stability of the Martian Atmosphere, *Science, 177,* 986-988

Nagy, A. F., A. Balogh, T. E. Cravens, M. Mendillo, I. Müller-Wodarg (Eds.) (2009), Comparative Aeronomy, ISBN 978-0-387-87824-9.

Parkinson, T. D., and Hunten, D. M. (1972), Spectroscopy and Acronomy of O_2 on Mars, *J. Atmos. Sci., 29,* 1380-1390

Pryor, W., J. Ajello, C. Barth, C. Hord, A. I. Stewart, K. Simmons, W. McClintock, B. Sandel, D. Shemansky (1992), The Galileo and Pioneer Venus ultraviolet spectrometer experiments – Solar Lyman-alpha latitude variation at solar maximum from interplanetary Lyman-alpha observations, *J. Astrophys., 394,* p. 363 – 377

Pryor, W.R., G. M. Holsclaw, W. E. McClintock, M. Snow, R. J. Vervack, G. R. Gladstone, S. A. Stern, K. D. Retherford, and P. F. Miles (2013), Lyman-alpha models for LRO LAMP based on MESSENGER MASCS and SOHO SWAN data, in "Cross-calibration of past and present far UV spectra of solar system objects and the heliosphere", ISSI Scientific Report N°13, E. Quemerais, M. Snow, R.-M. Bonnet eds., Springer.

Quemerais, E., and Bertaux, J. L. (1993), Radiative Transfer in the Interplanetary Medium at Lyman Alpha, *Astron. Astrophys., 277,* 283-301.

Rahmati, A. et al. (2017), MAVEN measured oxygen and hydrogen pickup ions: Probing the martian exosphere and neutral escape, *J. Geophys. Res., 122,* p. 3689-3706.

Rahmati, A. et al. (2018), Seasonal variability of neutral escape from Mars as derived from MAVEN pick-up ion observations, *J. Geophys. Res.: Planets, 123,* p. 1192-1202.

Romanelli, N. et al. (2016), Proton cyclotron waves occurance rate upstream from Mars observed by MAVEN: Associated variability of the martian upper atmosphere, *J. Geophys. Res., 121,* p. 11.

Stone, S., R. V. Yelle, M. Benna, M. Elrod, P. Mahaffy (2018), Thermal structure of the Martian upper atmosphere from MAVEN NGIMS, *J. Geophys. Res.: Planets, 123,* p. 2842-2867.

1146 Venot, O., Y. Bénilan, N. Fray, M.-C. Gazeau, F. Lefèvre, Et. Es-sebbar, E. Hébrard, M. Schwell,
1147 C. Bahrini, F. Montmessin, M. Lefèvre, I. P. Waldmann (2018), VUV-absorption cross section of
1148 carbon dioxide from 150 to 800 K and applications to warm exoplanetary exospheres, *Astron. &*
1149 *Astrophys., 609,* id.A34, 13 pp.

1150 Vidal-Madjar, A., and J. L. Bertaux (1972), A calculated hydrogen distribution in the exosphere,
1151 *Planet. & Sp. Sci., 20,* p. 1147-1162.

1152 Villanueva, G., Mumma, M., Novak, R., Käufl, H., Hartogh, P., Encrenaz, T., Tokunaga, A.,
1153 Khayat, A., Smith, M. (2015), Strong water isotopic anomalies in the martian atmosphere: Probing
1154 current and ancient reservoirs, Science, 348(6231), 218–221, doi:10.1126/science.aaa3630.